Journal of Medicinal Chemistry

pubs.acs.org/jmc

Article

Discovery of Nanomolar DCAF1 Small Molecule Ligands

Alice Shi Ming Li,[&] Serah Kimani,[&] Brian Wilson,[&] Mahmoud Noureldin, Héctor González-Álvarez, Ahmed Mamai, Laurent Hoffer, John P. Guilinger, Ying Zhang, Moritz von Rechenberg, Jeremy S. Disch, Christopher J. Mulhern, Belinda L. Slakman, John W. Cuozzo, Aiping Dong, Gennady Poda, Mohammed Mohammed, Punit Saraon, Manish Mittal, Pratik Modh, Vaibhavi Rathod, Bhashant Patel, Suzanne Ackloo, Vijayaratnam Santhakumar, Magdalena M Szewczyk, Dalia Barsyte-Lovejoy, Cheryl H. Arrowsmith, Richard Marcellus, Marie-Aude Guié, Anthony D. Keefe, Peter J. Brown,* Levon Halabelian,* Rima Al-awar,* and Masoud Vedadi*

Cite This: *J. Med. Chem.* 2023, 66, 5041−5060

Read Online

ACCESS | Metrics & More | Article Recommendations | Supporting Information

ABSTRACT: DCAF1 is a substrate receptor of two distinct E3 ligases ($CRL4^{DCAF1}$ and EDVP), plays a critical physiological role in protein degradation, and is considered a drug target for various cancers. Antagonists of DCAF1 could be used toward the development of therapeutics for cancers and viral treatments. We used the WDR domain of DCAF1 to screen a 114-billion-compound DNA encoded library (DEL) and identified candidate compounds using similarity search and machine learning. This led to the discovery of a compound (Z1391232269) with an SPR K_D of 11 μM. Structure-guided hit optimization led to the discovery of OICR-8268 (**26e**) with an SPR K_D of 38 nM and cellular target engagement with EC_{50} of 10 μM as measured by cellular thermal shift assay (CETSA). OICR-8268 is an excellent tool compound to enable the development of next-generation DCAF1 ligands toward cancer therapeutics, further investigation of DCAF1 functions in cells, and the development of DCAF1-based PROTACs.

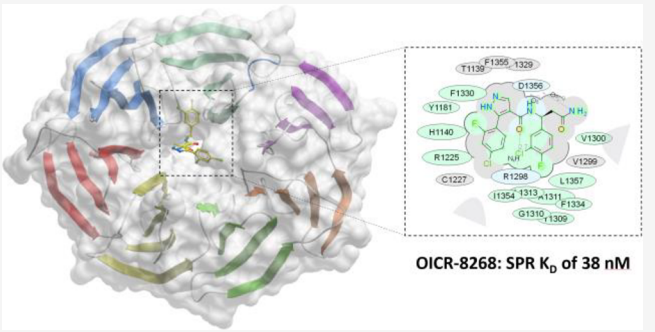

INTRODUCTION

Targeted protein degradation is an emerging therapeutic modality for the treatment of diseases, especially cancers.[1,2] Proteolysis targeting chimeras (PROTACs) are heterobifunctional molecules that consist of a chemical entity binding to the target protein linked to another chemical entity binding to an active E3 ubiquitin ligase. A PROTAC molecule brings together the target and E3 ligase into proximity and allows the E3 ubiquitin ligase to ubiquitinate the target protein and mark the target for protein degradation. The ubiquitin proteasome system is one of many mechanisms that regulate protein degradation in the cell. Protein degradation via the ubiquitin-26s proteasome system is a multistep process of covalently linking ubiquitin to substrate proteins. This process involves three classes of enzymes: ubiquitin-activating (E1), ubiquitin-conjugating (E2), and ubiquitin ligase (E3). There are more than 600 reported E3 ubiquitin ligases, and they can be grouped into different families such as the HECT domain containing, RING-finger containing, and RBR types.[3] Current PROTACs are mainly based on utilizing the E3 ligase complexes cereblon (CRBN) and von Hippel−Lindau (VHL). Although there are a few other E3 ligases, e.g., mouse double minute 2 homolog (MDM2), and inhibitors of apoptosis protein (IAPs) used in PROTACs, CRBN-based and VHL-based PROTACs are the most common.[4,5] Thus, additional E3 ubiquitin ligases could be explored with ligands designed to avoid limitations and expand the application of PROTACs.

Among the plethora of E3 ubiquitin ligases, the RING-type family is the largest E3 family. The RING-finger E3 family contains a subgroup called the cullin-RING ligases (CRLs).[6] CRLs are multi-subunit E3 ligase complexes that contain a cullin (CUL) protein, a RING protein, an adaptor protein, and a substrate receptor protein. There are a few reported adaptor proteins that CRLs utilize and are specific to each CUL such as the DNA damage binding protein 1 (DDB1), Skp1, and Elongin B/Elongin C.[7] For example, the CUL4A-DDB1-CRBN ($CRL4^{CRBN}$) complex has CRBN as the substrate recognition subunit for CUL4A through interaction with DDB1.[8] CRL4 also utilizes a class of substrate recognition

Received: December 30, 2022
Published: March 22, 2023

https://doi.org/10.1021/acs.jmedchem.2c02132
J. Med. Chem. 2023, 66, 5041−5060

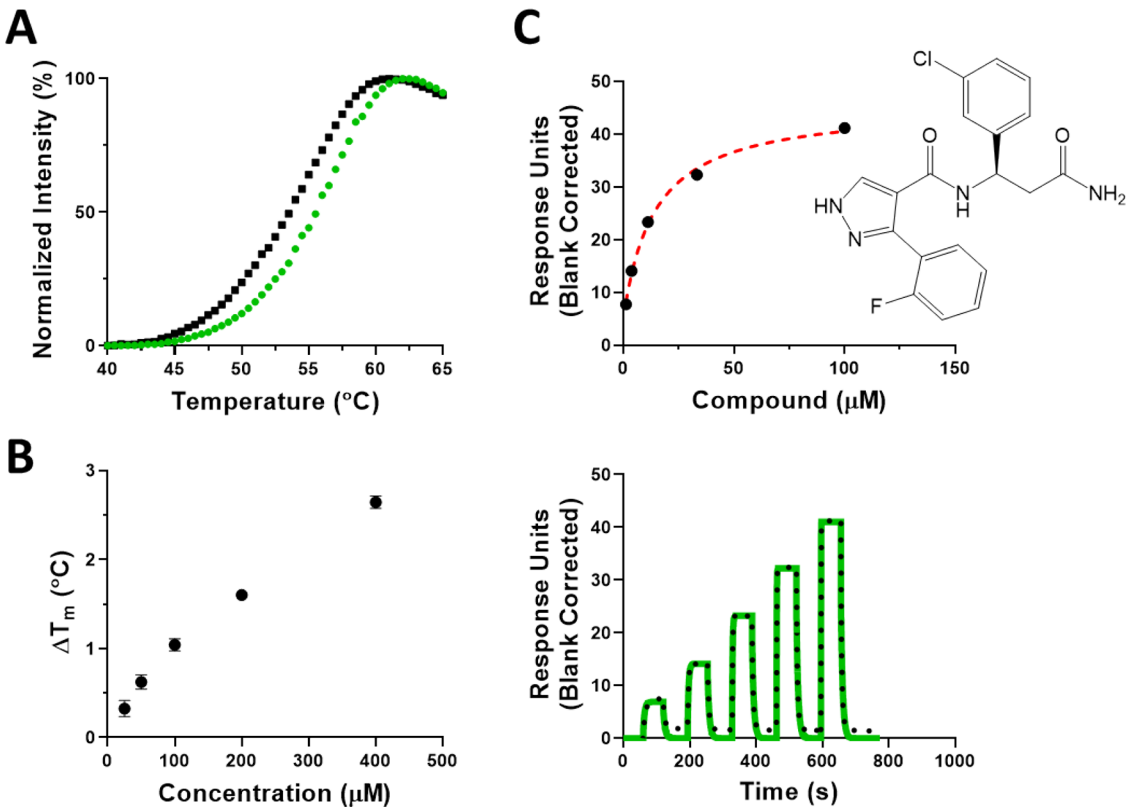

Figure 1. Confirmation of Z1391232269 binding to the DCAF1 WDR domain by biophysical methods. (A) Z1391232269 stabilized the WDR domain of DCAF1 at 400 μM (green trace) compared with the WDR domain with no compound (black trace), and (B) the effect was concentration dependent. (C) SPR confirmed its binding to DCAF1 with a K_D of 11.5 ± 4.2 μM. Experiments were performed in triplicate.

subunits called the DDB1-CUL4-associated factors (DCAFs).[7] DCAFs were first identified as WD40 repeat proteins from proteomic screens using tandem affinity purifications of DDB1 and CUL4A.[9−11] Among the DCAFs, DCAF1 is a substrate receptor in the CUL4A-DDB1-DCAF1 ($CRL4^{DCAF1}$) complex. Initially, DCAF1 was discovered as a target protein hijacked by the human immunodeficiency virus-1 (HIV-1) viral protein Vpr.[12] Hence, DCAF1 is also known as Vpr binding protein (VprBP). Vpr binds to DCAF1 to hijack the $CRL4^{DCAF1}$ E3 ligase complex to induce cell cycle arrest.[13] $CRL4^{DCAF1}$-Vpr also targets host proteins such as uracil DNA glycosylase 2 (UNG2),[14] endoribonuclease Dicer,[15] and histone deacetylase SIRT7[16] for ubiquitination leading to protein degradation. The co-crystal structure of DDB1-DCAF1-Vpr-UNG2 (PDB: 5jk7) reveals the detailed interactions on how Vpr mimics DNA binding to UNG2 for subsequent protein degradation.[17] Similarly, the Vpx protein of HIV-2/simian immunodeficiency virus hijacks the $CRL4^{DCAF1}$ complex recruiting SAMHD1, an HIV restriction factor for proteasome-dependent degradation.[18,19] These viruses utilize the $CRL4^{DCAF1}$ complex to modulate the cellular environment to prolong viral replication and pathogenesis.

Since its initial discovery, DCAF1 has been shown to be involved in various normal physiological functions in the cell. These functions include cell cycle regulation/progression, cell division, cellular proliferation, lipid metabolism, and miRNA biogenesis, among others.[20] Within these processes, DCAF1 is also a substrate recognition subunit for a different E3 ligase complex called EED-DDB1-VprBP (EDVP) where it plays a role in cytoskeletal organization and cell division.[21,22] It has been reported that Vpr hijacks the $EDVP^{DCAF1}$ complex to disrupt centrosome homeostasis.[23] Thus, DCAF1 is unique in which it can service two distinct E3 ubiquitin ligases.[20,24] DCAF1 also has an E3 ligase-independent function as it was shown to have kinase activity by phosphorylating histone H2A at Thr120.[25] H2AT120 phosphorylation (H2AT120p) by DCAF1 is associated with gene silencing at tumor suppressor genes,[25] and overexpression of DCAF1 and H2AT120p has been shown to cause proliferation of colon cancer cells.[26]

The diverse biological role of DCAF1 makes it an attractive target for drug discovery. We aimed to find small molecule ligands for DCAF1 to help further elucidate its roles in cells and to help enable the development of PROTAC molecules. DNA-encoded library (DEL) technology is a method to identify small molecule binders to a protein target, which has emerged as a popular screening approach in drug discovery. A DEL is a collection of small molecules each covalently linked to a unique DNA sequence that acts as a barcode for identification. The combination of DEL screening, machine learning, and large commercial synthetically accessible enumerate spaces is an alternative to traditional high-throughput screening as it enables the screening of billions of compounds at a fraction of the cost.[27]

We employed DEL technology to screen the WDR domain of DCAF1 by affinity-mediated selection and used the enrichment data to build machine learning models or conduct similarity searches to predict, optimize, and select commercially available small molecules for further testing. Here, we report the discovery and cellular target engagement of the first nanomolar DCAF1 ligand, OICR-8268, with an SPR K_D of 38 nM, and detailed structure-guided hit optimization. This discovery provides a basis for future development of

https://doi.org/10.1021/acs.jmedchem.2c02132
J. Med. Chem. 2023, 66, 5041−5060

DCAF1-based PROTACs and DCAF1 antagonists. In addition, OICR-8268 could be used as a chemical tool to further investigate DCAF1 functions in cells.

RESULTS AND DISCUSSION

Hit Generation from Machine Learning and Similarity Searching of DEL Screening Data. The WDR domain of DCAF1 (1038−1400) with N-terminal 6His-tag (hereafter referred to as DCAF1) was screened at X-Chem using a proprietary 114-billion-compound collection of 59 DNA-Encoded Chemical Libraries, and the data were processed by similarity searching and machine learning algorithms to purchase commercial compounds for assay evaluation as previously reported.[27,28] The 2D structure similarity searching workflow comprised searching the large commercially accessible EnamineREAL database (720 M) for 2D structures similar to representative enriched instances and truncates (see the Experimental Section). This led to the acquisition of a collection of 33 commercially available compounds that were evaluated by differential scanning fluorimetry (DSF; Figure S1) and surface plasmon resonance (SPR). From this initial set of 33 compounds, the commercially available compound (Z1391232269) was confirmed as a hit by both DSF and SPR assays. It stabilized DCAF1 with an increase in melting temperature (ΔT_m) greater than 2 °C in a concentration-dependent manner, indicating binding (Figure 1A,B). The binding was further confirmed with an SPR K_D value of 11.5 ± 4.2 μM (Figure 1C). Isothermal titration calorimetry (ITC) was also used as an additional orthogonal method and confirmed its binding with a K_D of 9 μM (Figure S2).

Analysis of the First Crystal Structure of DCAF1 in Complex with the Initial Hit Reveals a Sub-micromolar Enantiomer. Crystallization of DCAF1 in complex with Z1391232269 (**3c**) further confirmed its binding. However, the analysis of the structure (Figure S3) revealed a clear suboptimal geometry of the bound R-enantiomer (**3c**). Indeed, the torsion angle of the central amide function was distorted to about 90° to fit the electron density. Molecular modeling and docking experiments were performed to generate reasonable conformations of the ligand that fit the electron density. In parallel, the alternative S-enantiomer (**3d**) was also considered and was found to provide a better fit for the electron density with a near-optimal trans-conformation amide torsion angle.

Following this molecular modeling study, the pure enantiomers were resynthesized to further confirm our observations. The synthesis of these key analogs was carried out using standard EDCI coupling conditions as shown in Scheme 1. The coupling of the commercially available chiral β-amino amides **1** with the commercially available pyrazole carboxylic acids **2** afforded the target compounds **3** in modest (28−38%) yields.

Scheme 1. Synthesis of Compounds 3a and 3c−d[a]

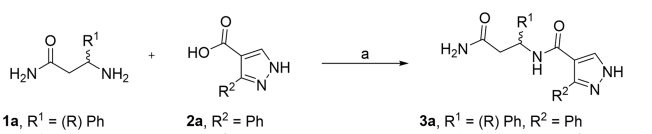

1a, R^1 = (R) Ph
1c, R^1 = (R) 3-Cl Ph
1d, R^1 = (S) 3-Cl Ph

2a, R^2 = Ph
2c, R^2 = 2-F Ph
2d, R^2 = 2-F Ph

3a, R^1 = (R) Ph, R^2 = Ph
3c, R^1 = (R) 3-Cl Ph, R^2 = 2-F Ph
3d, R^1 = (S) 3-Cl Ph, R^2 = 2-F Ph

[a]Reagents and conditions: (a) EDCI, DIEA, 0 °C (5 min), rt (18 h).

In SPR experiments, a significant difference in binding affinities of the enantiomers was observed (Table 1). These results, in combination with chiral HPLC analysis of **3c** and **3d**, provided an explanation for the structural observation. Indeed, chiral HPLC showed that compound **3c** was contaminated with a minor amount of the other enantiomer **3d**. This finding shed light on the discrepancies observed in the X-ray structure of DCAF1 and **3c**. Although the initial compound solution contained only about 4% **3d**, it was preferentially crystallized with the protein as a result of the ∼27-fold higher binding affinity (Table 1). Finally, small substitutions on both the northern and southern aromatic rings (**3d**, compared to unsubstituted compound **3b**) significantly improved potency.

Table 1. Structure−Activity Relationships of Compounds 3a−d

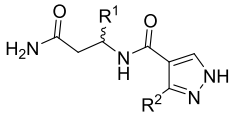

compound	R^1	R^2	DCAF1 K_D (nM)
3a	(R) Ph	Ph	NB[a]
3b	(S) Ph	Ph	16,400; 16,900[b]
3c	(R) 3-Cl Ph	2-F Ph	13,500 ± 200
3d	(S) 3-Cl Ph	2-F Ph	490 ± 90

[a]NB = no binding. [b]This experiment was performed in duplicate.

To confirm our molecular modeling predictions, **3d (S-enantiomer)** was synthesized as a pure enantiomer. Our SPR data confirmed that compound **3d (S-enantiomer)** has a higher affinity for binding to DCAF1 (Figure 2A) with a K_D of 490 ± 90 nM compared to compound **3c (R-enantiomer)** with a K_D of 13.5 ± 0.2 μM. The observed trend of this set of compounds indicated that S-isomers were more potent DCAF1 binders. Similarly, in the DSF experiments (Figure 2B), **3d** showed DCAF1 stabilization at 25 μM, but **3c** did not show any significant effect even at 50 μM. As an additional orthogonal confirmation, ITC experiments confirmed binding of compound **3d** to DCAF1 with an ITC K_D value of 932 ± 150 nM (Figure 2C). The binding interaction between **3d** and DCAF1 is enthalpy-driven and exothermic with an enthalpy (ΔH) of −64.1 ± 1.5 kJ/mol and entropy (ΔS) of −99.5 ± 6.0 J/mol·K.

Crystal Structure of the Human DCAF1 WDR Domain Bound to 3d. The human DCAF1 WDR domain (residue range 1077 to 1390) was used in crystallization experiments, in which residues 1077 and 1079 were mutated to alanine to promote crystallization. A new DCAF1 co-crystal structure in complex with compound **3d (S-enantiomer)**, referred to here as DCAF1-**3d** (PDB ID: 7UFV), was determined to 1.9 Å resolution in $P12_11$ space group symmetry. There are two molecules in the crystal asymmetric unit, and most residues were well resolved, except residues 1315−1325 and 1374−1378 in chain A and residues 1316−1326 and 1373−1379 in chain B. Table 2 summarizes the crystallographic data collection, refinement, and validation statistics.

A well-defined electron density map was observed for the entire **3d** molecule in both chains of the crystal asymmetric unit (Figure S4), which confirmed the modeled S-enantiomer binding mode (RMSD of 0.5 Å). Thus, we concluded that the original structure of the protein−ligand complex was based on

https://doi.org/10.1021/acs.jmedchem.2c02132
J. Med. Chem. 2023, 66, 5041−5060

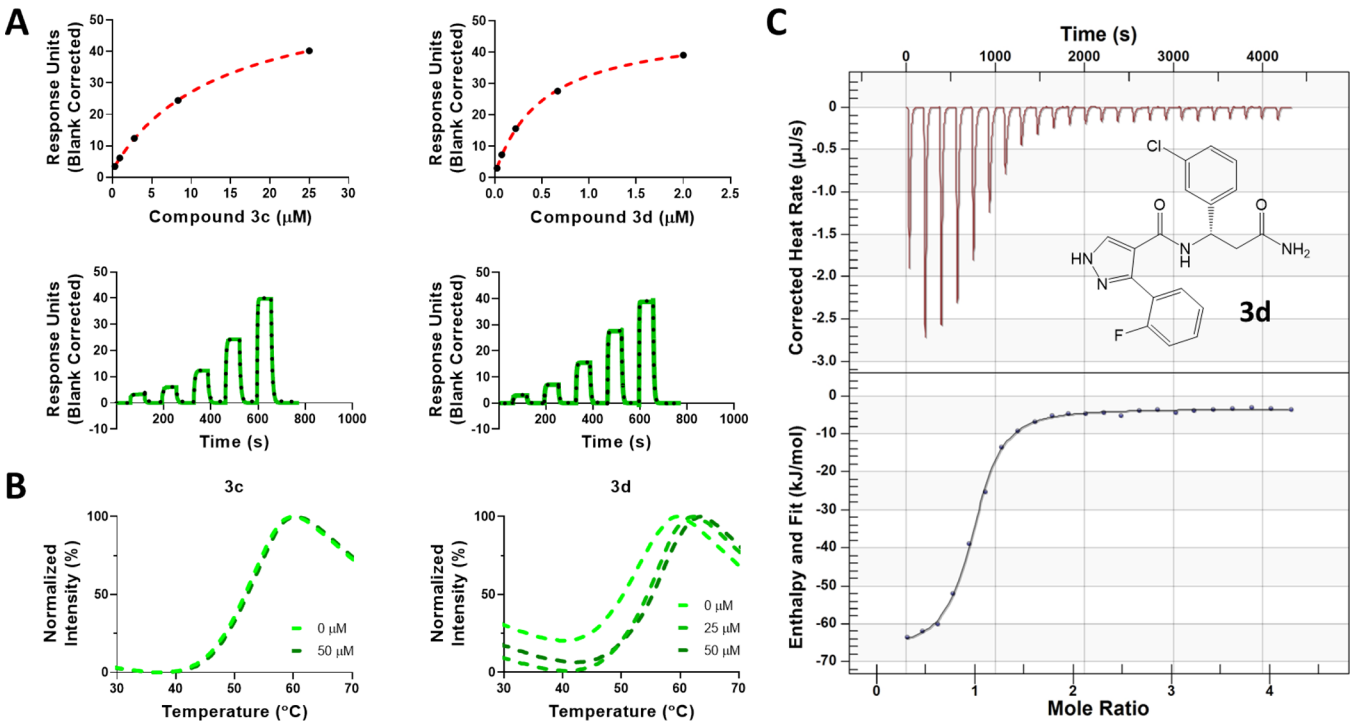

Figure 2. Biophysical characterization of compounds **3c** and **3d**. Binding of compound **3c** and **3d** to DCAF1 WD40 domain was assessed using (A) SPR (K_D values of 490 ± 90 nM for **3d** and 13.5 ± 0.2 μM for **3c**) and (B) DSF (ΔT_m of 2.8 ± 0.05 and 3.8 ± 0.08 °C at 25 and 50 μM for **3d**, respectively, and no stabilization effect for **3c** even at 50 μM). Compound **3d** was orthogonally confirmed by (C) ITC with a K_D value of 932 ± 150 nM. The chemical structure of **3d** is shown. Experiments were performed in triplicate.

an enantiomerically impure mixture (92% ee (R)) and the S-enantiomer preferentially co-crystallized with the protein because of its higher affinity for DCAF1.

Compound **3d** is nestled deep inside the central tunnel of the DCAF1 WDR domain, where it appears to be positioned slightly off center (Figure 3A). It makes extensive hydrogen bonding as well as hydrophobic interactions with residues lining the central tunnel of the DCAF1 WDR domain ring (Figure 3B). Specifically, the central amide group of **3d** forms hydrogen bonding interactions with the side chain of Asp1356 and another with the guanidinium group of Arg1298 on the opposite side. The pyrazole ring on the other hand is involved in edge-to-face aromatic interaction with the side chain of Phe1330 and coordinates a nearby water molecule (HOH04). The 3-chlorophenyl group is nestled in a hydrophobic pocket composed of Leu1357, Ile1354, Phe1330, Ala1311, and Val1300 and forms π-stacking interaction with the aromatic ring of Phe1330. In chain A, the terminal amide group of **3d** interacts with the imidazole ring of His1140 through hydrogen bonds (Figure 3B).

Comparison of the DCAF1-**3d** structure with that of human DCAF1 in complex with the lentiviral accessory protein Vpx and the Mandrill SAMHD1 (PDB ID: 5AJA) reveals that the compound binds at a site distant from the Vpx peptide binding site and does not overlap with it (Figure 3C). Although compound **3d** may not be able to displace the Vpx protein, it could be further optimized by extending it toward the surface of the central pore to disrupt the interaction of DCAF1 with its binding partners.

Methylation of the Pyrazole Core and Amide Modification. With the preferred stereochemistry established, we investigated the impact of *N*-alkylation of the core pyrazole. With modest yields obtained in EDCI coupling reactions, we explored an alternative coupling protocol using MsCl and DIEA (Scheme 2). This protocol afforded **5b** in improved yield; however, when applied to the synthesis of **5a**, the result was a complex mixture of products and a lower yield. These reaction conditions did not offer any advantage over the standard EDCI coupling conditions used to synthesize the majority of the compounds described in this manuscript. The synthesis of *N*-Me amide analog **5c** is illustrated in Scheme 3. HATU coupling of methylamine with Boc protected acid **6** afforded **7** in excellent yield. Deprotection of **7** with HCl in 1,4-dioxane afforded the methylated coupling partner **8** also in excellent yield. Variability in the key final coupling reaction of unprotected pyrazole acids **2** with β-amino amides **1** encouraged us to investigate protection of the pyrazole before amide formation. Tosylation of **2a** afforded **9** (35% yield), and subsequent HATU coupling (55% yield) and deprotection afforded **5c** in 51% yield. Although the yields of the individual reactions of this synthetic scheme were somewhat disappointing, this alternative route could provide access to targets otherwise inaccessible without pyrazole protection. The primary amide in **3d** was also dehydrated to the nitrile under standard conditions to afford **5d**.

As shown in Table 3, both possible methylated pyrazoles **5a** and **5b** exhibited reduced affinity for DCAF1 when compared to **14c**. Molecular modeling predicted that this ring decoration (**5a**) would be detrimental for activity. Indeed, the small hydrophobic methyl group would be surrounded by backbone polar groups from several protein residues (Thr1097, Thr1139, and Phe1355). Also, this methyl group would perturb a water-mediated hydrogen bond network: a key water molecule, which mediated hydrogen bonds between the pyrazole core and backbone from residues Thr1097 and Thr1139, would be displaced. Similarly, the alternative tautomer (**5b**) was

https://doi.org/10.1021/acs.jmedchem.2c02132
J. Med. Chem. 2023, 66, 5041−5060

Table 2. Data Collection and Refinement Statistics[a]

	DCAF1-3d	DCAF1-26e
PDB ID	7UFV	8F8E
	Data collection	
wavelength (Å)	0.97911	0.97918
space group	$P12_11$	$P12_11$
cell dimensions		
a, *b*, *c* (Å)	49.140, 87.875, 73.807	48.865, 88.084, 73.562
α, β, γ (°)	90.00, 98.54, 90.00	90.00, 97.56, 90.00
resolution range (Å)	43.94−1.90 (1.94−1.90)	44.08−1.55 (1.58−1.55)
total reflections	184,284	470,878
unique reflections	48,379 (3107)	171,794 (8612)
multiplicity	3.80 (3.80)	2.7 (2.6)
completeness (%)	99.0 (99.5)	97.2 (97.4)
mean *I*/sigma(*I*)	9.6 (1.5)	19.7 (1.25)
R-merge	0.062 (0.923)	0.061 (0.677)
R-meas	0.072 (1.070)	0.076 (0.836)
R-pim	0.036 (0.534)	0.044 (0.486)
CC1/2	0.998 (0.726)	0.996 (0.658)
	Refinement	
reflections used in refinement	46,002 (3420)	86,348 (6249)
reflections used for R-free	2355 (145)	1744 (118)
R-work	0.2041 (0.365)	0.1812 (0.273)
R-free	0.2542 (0.334)	0.2089 (0.293)
number of nonhydrogen atoms		
all atoms	4696	5136
macromolecules	4580	4764
ligands	55	71
solvent	88	330
RMSDs		
bond lengths (Å)	0.0065	0.0072
angles (°)	1.2412	1.4212
average B factors (Å2)		
macromolecule	47.162	25.160
ligands/ions	42.921	24.459
solvent	42.320	32.068
	Validation	
Ramachandran plot (%)		
favored	95.49	97.6
allowed	100	100
outliers (%)	0.0	0.0
Clashscore	3.5	1.61
rotamer outliers (%)	0.0	0.78

[a]Statistics for the highest-resolution shell are shown in parentheses.

predicted to be even less potent because it would create hydrogen-bond acceptor mismatches between the decorated pyrazole ring and the constrained water molecules. Indeed, both hydrogen bond donor features from solvent molecule were already engaged in polar interactions with the carbonyl backbone group from Thr1097 and Thr1139.

Methylation of the primary amide **5c** was also detrimental to affinity when compared to **3b**. As for the methylated pyrazole case, it was predicted that this modification would perturb a water-mediated hydrogen bond network in the vicinity of Cys1099, His1140, and Asp1356 residues. Finally, the primary amide **3d** to nitrile **5d** conversion was also detrimental to affinity with about 6-fold loss in potency.

This second set of compounds highlighted that the SAR landscape is sensitive for this series, as exemplified by several activity cliffs with minor structural changes.

Northern Phenyl Ring Optimization. Exploring the substitution of the "northern" phenyl ring was accomplished using EDCI coupling as the final step (Scheme 4). Although yields of products were low to modest (9−45%), the operational simplicity of this reaction between pyrazole acid **2a** and β-amino amides **1d−m** provided rapid access to the desired compounds **14a−j** for testing. Amino amides that were not commercially available **1h−i** and **1k−m** were prepared in three steps from the corresponding commercial β-amino acids **11** (Scheme 4).

As shown in Table 4 the presence of the northern aromatic ring is required for activity (**14a**). Analysis of the crystal structure revealed that the binding pocket that accommodates the northern phenyl ring is very deep and hydrophobic. Indeed, this pocket is delimited by V1299, V1300, Y1309, G1310, A1311, F1330, I1354, and L1357 residues. As expected, all favorable modifications concerned the decoration of the aromatic ring with halogen substituents at various positions. Thus, large halogens at the meta-position significantly improved potency (**3d**, **14c**). Indeed, the chlorine atom is located at optimal Van der Waals distances (3.6−4.0 Å) to several hydrophobic sidechains from the pocket. Surprisingly, the meta fluorine substituted analog (**14f**) displayed no binding, whereas the unsubstituted ring still showed some activity (**3b**). Similarly, para substitutions were also predicted to have favorable impact on potency. Thus, fluorine (**14g**) and chlorine (**14d**) analogs exhibited improved affinity for DCAF1 compared to the unsubstituted northern phenyl ring (**3b**).

Analysis of the X-ray structure was able to explain why the ortho modifications such as **14b**, **14e**, and **14h** were either suboptimal or even expected to be detrimental for potency (small available space to accommodate chemical moieties and potential intramolecular clashes preventing the observed bioactive conformation). The least sterically demanding ortho fluoro (**14e**) analog was tolerated but offered no improvement when compared to the unsubstituted (**3b**) analog. Substitution of the aromatic ring with alkoxy substituents in either the *ortho* **14h**, *meta* **14i**, or *para* **14j** position was also not tolerated.

Southern Phenyl Ring Optimization. A complementary exercise was conducted to determine the optimal substitution for the southern phenyl ring. The effect on substitutions on the biaryl phenyl ring was explored systematically by keeping all other positions constant. The final compounds were purchased if available or synthesized by EDCI coupling of **1b** with **2** (Scheme 5).

Similar to the northern phenyl, the presence of the southern aromatic ring is required for activity **15a** (Table 5). As for the northern ring, the binding pocket that accommodates the southern phenyl ring is also hydrophobic. Indeed, this cavity is delimited by His1140, Tyr1181, Arg1225, Cys1227, Arg1298, Leu1313, Pro1329, and Phe1330 residues. However, the binding pocket is not deeply buried anymore and contains two polar arginine residues. Again, all favorable modifications concerned the decoration of the aromatic ring with halogen substituents at varied positions. Notably, addition of halogen atoms at the ortho position showed favorable impact on potency (**15b** and **15e** compounds compared to **3b**) because we speculate that the ortho substituents can now promote a non-coplanar angle between the two rings. Also, this bioactive

https://doi.org/10.1021/acs.jmedchem.2c02132
J. Med. Chem. 2023, 66, 5041−5060

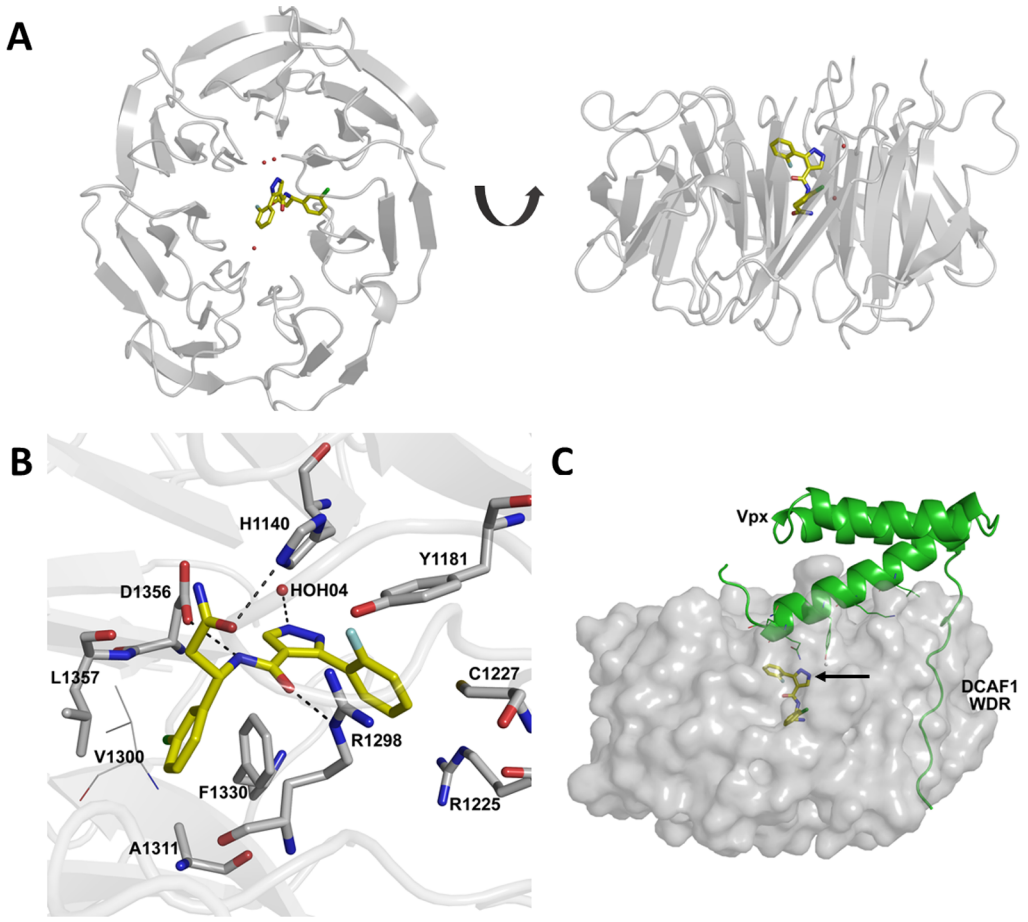

Figure 3. Co-crystal structure of DCAF1 WDR domain in complex with compound **3d**. (A) The top and side views of the DCAF1 WDR domain shown as cartoon representation in gray bound to **3d** shown as yellow sticks. (B) Close-up view of the **3d** binding site in chain A of DCAF1-**3d**. **3d** forms a network of interactions with the protein and a water molecule within the central channel of DCAF1 WDR domain ring. The compound is shown as yellow sticks, and the protein residues involved in the interactions are rendered as gray sticks. The hydrogen bonds are shown as black dashes, and an interacting water molecule is shown as a red sphere. (C) An overlay of the DCAF1-**3d** structure (shown in surface representation in light gray and **3d** in yellow sticks indicated by black arrow) onto the DCAF1 WDR domain in complex with lentiviral Vpx (shown in cartoon representation in green) and SAMHD1 (not shown) (PDB ID: 5AJA), showing the compound binding site relative to that of Vpx.

Scheme 2. Synthesis of Compounds 5a–b[a]

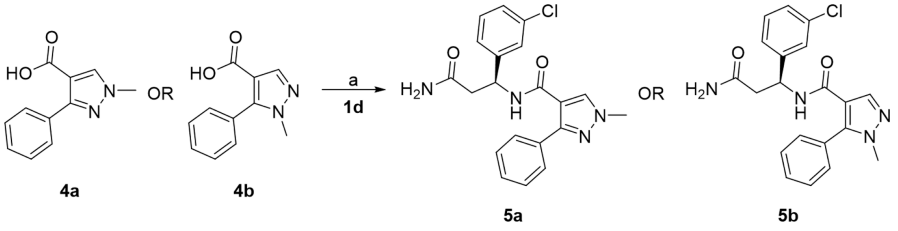

[a]Reagents and conditions: (a) MsCl, DIEA, DCM, 0 °C (10 min), then **1d**, 0 °C (30 min).

conformation exhibited cation-π interactions with a co-planar arginine residue in the vicinity of the southern ring. By contrast, halogenation at the meta position was tolerated but offered no real improvement (**15c**, **15f**), and *m*-cyano analog **15i** displayed ∼1.5-fold loss in potency. Para modifications on the southern ring displayed varied results: whereas both methoxy **15h** and fluoro **15g** analogs were poor, the very close chloro analog **15d** exhibited 5-fold potency gain with the addition of a single atom. This result can be explained by the favorable interaction between the chlorine atom from the ligand and the carbonyl backbone atom from Arg1225 (distance (Cl-O) = 3.3 Å, angle = 167° according to the model and confirmed by the second X-ray structure).[29]

Northern–Southern Combinations. Combining the findings from the northern and southern SAR studies for finding an optimal compound required an alternate synthetic pathway. Exploring specific and multiple substitutions of both aromatic rings required that we prepare specific enantiomerically enriched β-amino amides **1** and also assemble non-commercially available 3-phenyl pyrazole acids **2**. The addition of a Reformatsky reagent to an *N-tert*-butanesulfinyl imine **17** (Scheme 6) has been reported to proceed in high yield and excellent diastereoselectivity. Subsequent amidation and

https://doi.org/10.1021/acs.jmedchem.2c02132
J. Med. Chem. 2023, 66, 5041–5060

Scheme 3. Synthesis of Compound 5c[a]

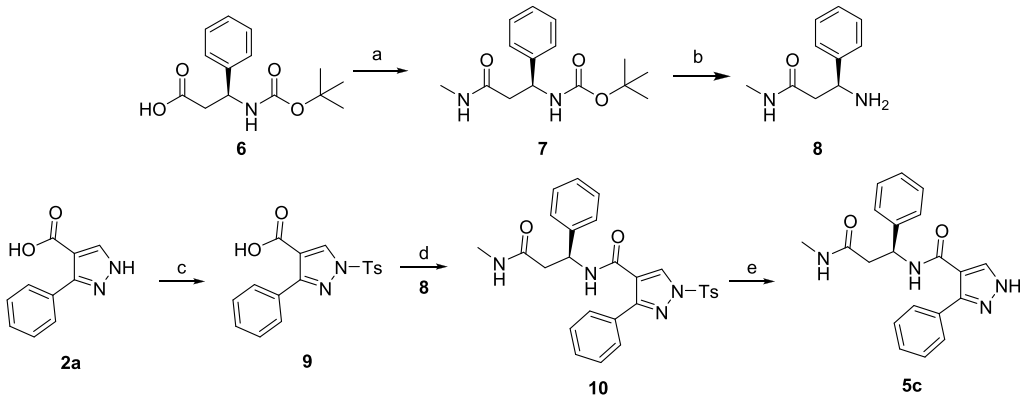

[a]Reagents and conditions: (a) HATU, DIEA, DMF, $MeNH_2$; (b) HCl in 1,4-dioxane; (c) TsCl, Py; (d) HATU, DIEA, DMF, **8**; (e) KOH (aq.), THF.

Table 3. Structure−Activity Relationships of Compounds 5a−d

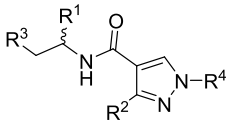

compound	R^1	R^2	R^3	pyrazole	DCAF1 K_D (nM)[a]
5a	(S) 3-Cl Ph	Ph	CO_2NH_2	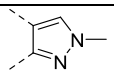	10,000; 9900
5b	(S) 3-Cl Ph	Ph	CO_2NH_2	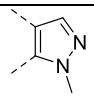	> 50,000
5c	(S) Ph	Ph	CO_2NHMe	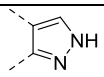	NB
5d	(S) 3-Cl Ph	2-F Ph	CN		2890; 2910

[a]Experiments were performed in duplicate.

deprotection afforded the desired intermediates **1** in high enantiomeric excess.

We envisioned that the desired substitution patterns in the southern phenyl ring could be obtained from the palladium catalyzed cross-coupling of the appropriate boronate **22** with the protected bromo-pyrazole ester **21** (Scheme 7). SEM protection of **20** afforded **21** as a mixture of regioisomers (the presumed major regioisomer is drawn) that efficiently underwent Suzuki cross-coupling with commercial boronic acids **22** under microwave irradiation. Saponification of **23** with KOH yielded the pyrazole acid intermediates **24** that coupled smoothly with β-amino amides **1** to afford protected intermediates **25**. Treatment of the silyl protected intermediates with TFA afforded the target compounds **26** in high purity but low yield after preparative chromatography.

Combining the best substituents on the northern and southern aromatic rings had a dramatic improvement of potency (Table 6). Halogens in both the 3 and the 4 positions of the northern ring (**26a**, **26b**) improved potency ∼2 fold over **3d**. Similarly, halogens in the 2 and the 4 position of the southern ring (**26c**, **26d**) provided an additional 1.5- to 5-fold boost in binding affinity for DCAF1. The observed increase in affinity was additive with compound **26e** being the most potent compound in this series.

Biophysical Characterization and Co-crystal Structure of Compound 26e with DCAF1. Compound **26e** showed the highest affinity for binding to the DCAF1 WDR domain with an SPR K_D value of 38 ± 1.5 nM (Figure 4A). DCAF1 was also significantly stabilized in the presence of **26e** (Figure 4B) in a concentration-dependent manner (Figure 4C) with a ΔT_m of 7.4 ± 0.5 °C at 100 μM (Table S1). DCAF1 stabilization of **26e** was higher than that for **3d** and correlated well with the potency of binding as measured by SPR. Additionally, ITC experiments confirmed **26e** binding to DCAF1 with a K_d value of 216 ± 76 nM. The binding interaction was enthalpy-driven and exothermic with a ΔH value of −50.4 ± 1.7 kJ/mol and ΔS value of −41.1 ± 3.9 J/mol·K.

The DCAF1 co-crystal structure in complex with compound **26e**, referred to here as DCAF1-**26e** (PDB ID: 8F8E), was

https://doi.org/10.1021/acs.jmedchem.2c02132
J. Med. Chem. 2023, 66, 5041−5060

Scheme 4. Synthesis of Compounds 14a–j[a]

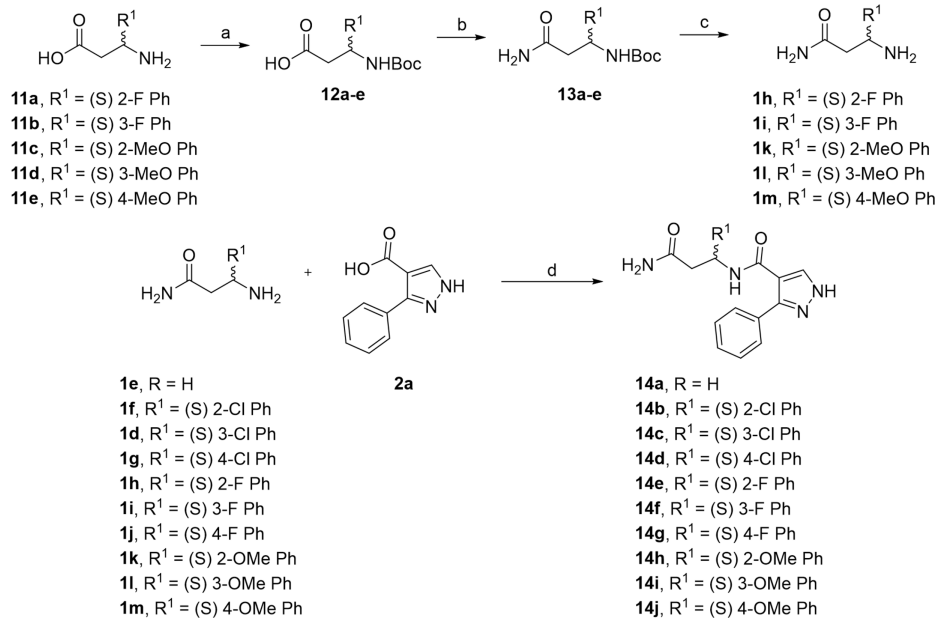

11a, R^1 = (S) 2-F Ph
11b, R^1 = (S) 3-F Ph
11c, R^1 = (S) 2-MeO Ph
11d, R^1 = (S) 3-MeO Ph
11e, R^1 = (S) 4-MeO Ph

1h, R^1 = (S) 2-F Ph
1i, R^1 = (S) 3-F Ph
1k, R^1 = (S) 2-MeO Ph
1l, R^1 = (S) 3-MeO Ph
1m, R^1 = (S) 4-MeO Ph

1e, R = H
1f, R^1 = (S) 2-Cl Ph
1d, R^1 = (S) 3-Cl Ph
1g, R^1 = (S) 4-Cl Ph
1h, R^1 = (S) 2-F Ph
1i, R^1 = (S) 3-F Ph
1j, R^1 = (S) 4-F Ph
1k, R^1 = (S) 2-OMe Ph
1l, R^1 = (S) 3-OMe Ph
1m, R^1 = (S) 4-OMe Ph

14a, R = H
14b, R^1 = (S) 2-Cl Ph
14c, R^1 = (S) 3-Cl Ph
14d, R^1 = (S) 4-Cl Ph
14e, R^1 = (S) 2-F Ph
14f, R^1 = (S) 3-F Ph
14g, R^1 = (S) 4-F Ph
14h, R^1 = (S) 2-OMe Ph
14i, R^1 = (S) 3-OMe Ph
14j, R^1 = (S) 4-OMe Ph

[a]Reagents and conditions: (a) BOC_2O, DIEA, DCM; (b) EDCI, NH_4Cl, DIEA, DCM; (c) HCl in 1,4-dioxane; (d) EDCI, DIEA, DCM 0 °C (5 min), rt (18 h).

Table 4. Structure–Activity Relationships of Compounds 14a–j

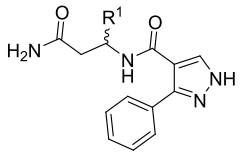

compound	R^1	DCAF1 K_D (nM)[a]
14a	H	NB
3b	(S) Ph	16,400; 16,900
14b	(S) 2-Cl Ph	22,960; 21,940
14c	(S) 3-Cl Ph	4220; 4000
14d	(S) 4-Cl Ph	6900; 6800
14e	(S) 2-F Ph	15,500; 15,800
14f	(S) 3-F Ph	NB
14g	(S) 4-F Ph	9600; 9800
14h	(S) 2-OMe Ph	NB
14i	(S) 3-OMe Ph	NB
14j	(S) 4-OMe Ph	NB

[a]Experiments were performed in duplicate.

Scheme 5. Synthesis of Compounds 15a–b, 15f, 15j[a]

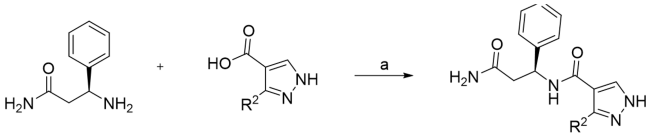

1b

2e, R^2 = Me
2f, R^2 = (S) 2-Cl Ph
2g, R^2 = (S) 3-F Ph
2h, R^2 = (S) 3-Cl 4-F Ph

15a, R^2 = Me
15b, R^2 = (S) 2-Cl Ph
15f, R^2 = (S) 3-F Ph
15j, R^2 = (S) 3-Cl 4-F Ph

[a]Reagents and conditions: (a) EDCI, DIEA, 0 °C (5 min), rt (18 h).

determined to 1.55 Å resolution in $P12_11$ space group symmetry with two molecules in the crystal asymmetric unit.

Table 5. Structure–Activity Relationships of Compounds 15a–j

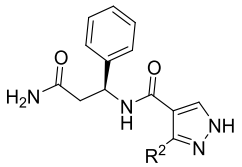

compound	R^2	DCAF1 K_D (nM)[a]
15a	Me	NB
3b	Ph	16,400; 16,900
15b	2-Cl Ph	4000; 4100
15c	3-Cl Ph	11,100; 11,200
15d	4-Cl Ph	2890; 2890
15e	2-F Ph	3400; 3420
15f	3-F Ph	15,700; 15,700
15g	4-F Ph	13,280; 12,960
15h	4-OMe Ph	35,100; 34,700
15i	3-CN Ph	24,900; 26,500
15j	3-Cl, 4-F Ph	15,900; 15,800

[a]Experiments were performed in duplicate.

Table 2 summarizes the crystallographic data collection, refinement, and validation statistics. A well-defined electron density map corresponding to **26e** was observed in both chains of the crystal asymmetric unit (Figure S5). As expected, **26e** binds in the same position deep inside the central pore as **3d**, maintaining all the previously observed interactions with the protein and a water molecule (Figure 5). Two additional water molecules coordinate with the compound: one (HOH160) with the N1 atom of the pyrazole ring and the second (HOH292) with the O1 atom of the terminal amide. The added fluoride atom in the 3-chloro-4-fluorophenyl group does not significantly affect the conformation of the protein residues, but it likely contributes to hydrophobic interactions within the hydrophobic pocket involving Leu1357, Ile1354,

https://doi.org/10.1021/acs.jmedchem.2c02132
J. Med. Chem. 2023, 66, 5041–5060

Scheme 6. Synthesis of Intermediates 1n−o[a]

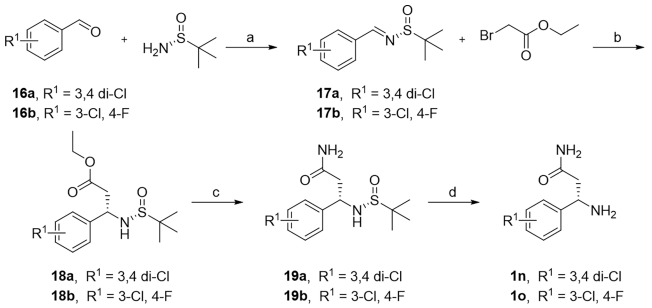

[a]Reagents and conditions: (a) PPTS, $MgSO_4$, DCM; (b) Zn, CuCl, THF; (c) 7 N NH_3 in MeOH; (d) HCl in 1,4-dioxane.

Phe1330, Ala1311, and Val1300. On the other hand, the added chlorine atom in the 2-fluoro-4-chlorophenyl group contributes to hydrophobic interactions with the protein by packing against the side chains of Arg1225 and Cys1227 (Figure 5). The side chain of Arg1225 adopts a different conformation in the DCAF1-**3d** structure (Figure 5B). As expected, the binding mode of the ligand (RMSD < 0.5 Å) and the overall binding site conformation have been perfectly conserved through the optimization process. Binding modes of ligands are displayed in Figure 6. Notably, the crystal structure of **26e** in complex with DCAF1 protein supported the halogen bond hypothesis, and this special interaction has been automatically detected by the 2D interaction diagram software (LID from Schrodinger).

Target Engagement of 26e and 3d. To confirm target engagement in cells, we generated a DCAF1 cellular thermal shift assay (CETSA) using NanoLuc split luciferase technology (Promega), in which we have produced stable H460 cells expressing the DCAF1 WDR domain or DCAF1 full-length tagged with a small fragment of NanoLuc luciferase (HiBit) that, upon complementation with the larger fragment of NanoLuc, will result in luminescence.[30] This approach allows the assessment of DCAF1 stability upon compound treatment by monitoring the change in denaturation temperature. Using this approach, **26e** significantly (>2 °C) stabilized HiBiT-DCAF1-WDR at 40 μM (Figure 7A, C) and was also dose-dependent (Figure 7B, D). Furthermore, **26e** thermally stabilized the WDR domain of DCAF1 to a greater extent than **3d,** with an EC_{50} value of 10.5 μM (Figure 7C,D). However, both compounds failed to thermally stabilize the full-length DCAF1 (HiBiT-DCAF1_FL) at 40 μM (Figure S6). This may simply be the case that binding of **26e** to the WDR domain of DCAF1 does not result in significant and detectable stabilization of the full-length protein (169 kDa).

Table 6. Structure−Activity Relationships of Compounds 26a−e

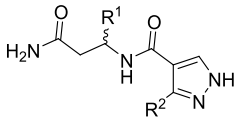

compound	R^1	R^2	DCAF1 K_D (nM)
26a	(S) 3-Cl, 4-F Ph	2-F Ph	170; 180
26b	(S) 3,4 di-Cl Ph	2-F Ph	200; 217
26c	(S) 3-Cl Ph	2,4-F Ph	265; 282
26d	(S) 3-Cl Ph	2-F, 4-Cl Ph	85 ± 10
26e	(S) 3-Cl, 4-F Ph	2-F, 4-Cl Ph	38 ± 1.5

Potential Applications of 26e. The biophysical characterization data showed high affinity binding of **26e** to DCAF1. In addition, the co-crystal structures revealed that the compound is buried deep into the central pore of the WD domain. The structural comparison with the Vpx peptide did not show any overlap with the compound, minimizing the possibility of direct antagonism. Most recently, an azetidine acrylamide-based electrophilic PROTAC for DCAF1 was reported.[31] This covalent DCAF1-based PROTAC specifically reacts with the cysteine 1113 of DCAF1 leading to degradation of FKBP12 and BRD4 by ectopically expressed, but not endogenous, DCAF1.[31] **26e**, however, is a reversible DCAF1 ligand with high affinity and cellular engagement. Therefore, it is an excellent starting tool for development of chemical handles for DCAF1-based PROTACs for degradation of desired targets. In addition, it could be further developed to

Scheme 7. Synthesis of Compounds 26a−e[a]

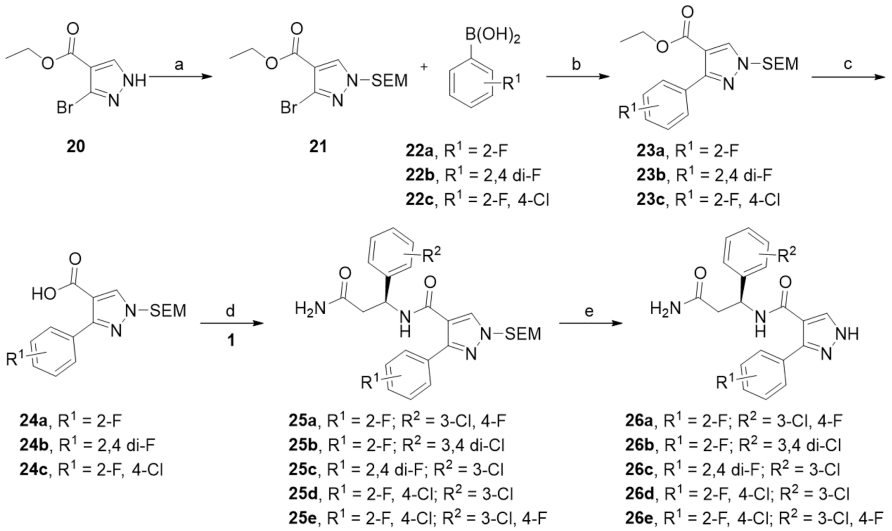

[a]Reagents and conditions: (a) NaH, SEMCl, THF; (b) $PdCl_2(PPh_3)_2$, Cs_2CO_3, 1,4-dioxane, H_2O, μw, 110 °C; (c) KOH, THF/MeOH/H_2O, 70 °C; (d) HATU, DIEA, DMF; (e) TFA, DCM.

https://doi.org/10.1021/acs.jmedchem.2c02132
J. Med. Chem. 2023, 66, 5041−5060

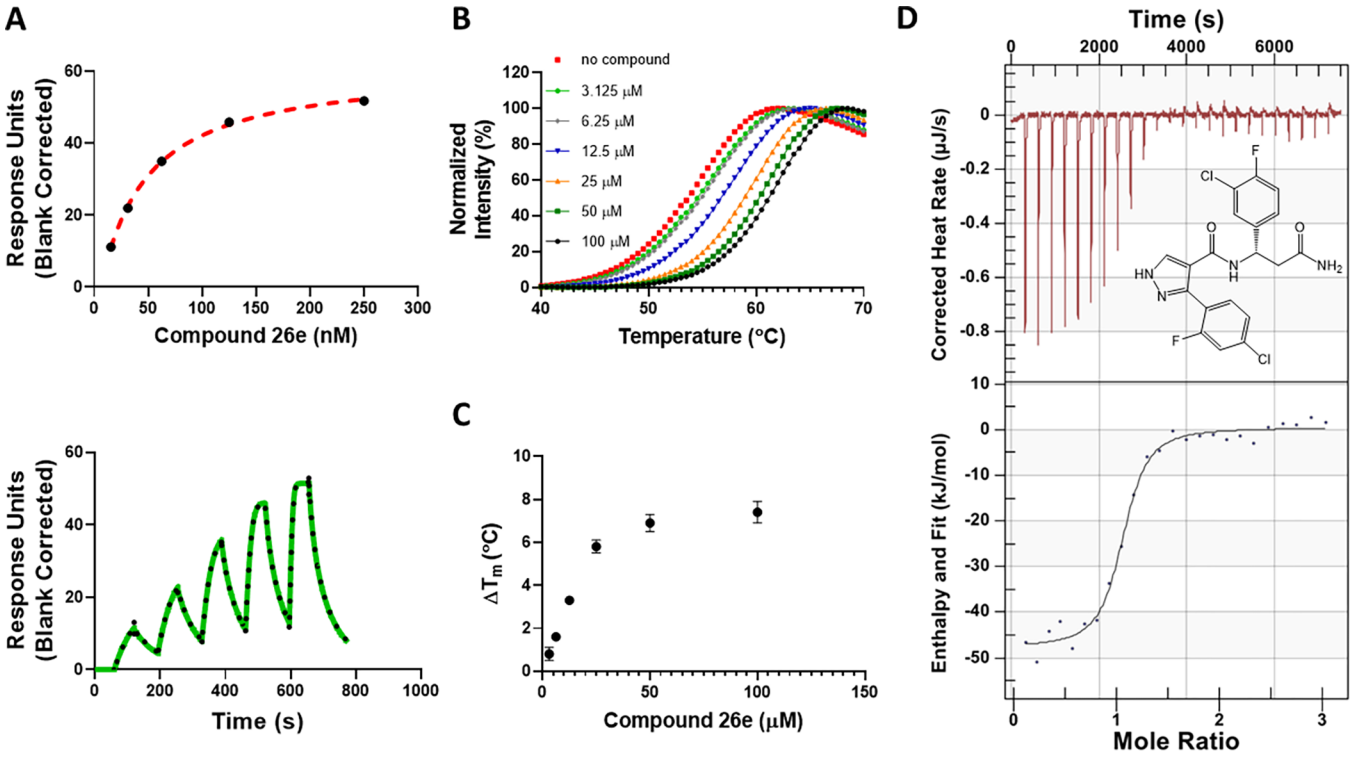

Figure 4. Biophysical characterization of compound **26e** (OICR-8268) with the DCAF1 WDR domain. Binding of compound **26e** to the DCAF1 WDR domain was tested by SPR and DSF assays. (A) SPR showed **26e** binding to DCAF1 potently with a K_D of 38 ± 1.5 nM, and (B) DSF showed that the compound stabilizes DCAF1 in a concentration-dependent manner (C) with increases in the protein's melting temperature, indicating binding. (D) Orthogonal binding confirmation of **26e** by ITC with a K_D of 216 ± 76 nM. All experiments were performed in triplicate.

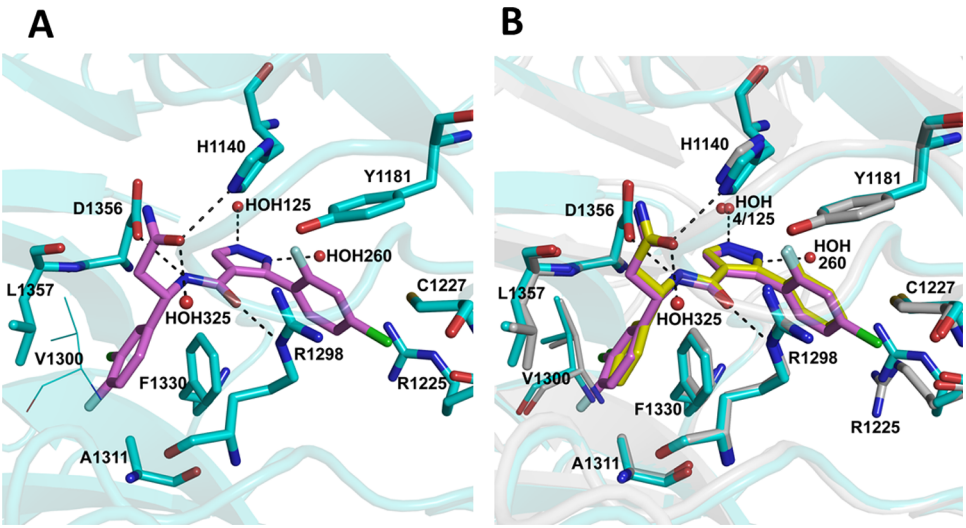

Figure 5. Co-crystal structure of DCAF1 WDR domain in complex with **26e**. (A) A close-up view of **26e** binding site in the central tunnel of the DCAF1 WDR domain. Compound **26e** retains the network of interactions observed in DCAF1-**3d** (Figure 3B) but also makes additional interactions with two extra water molecules, as well as additional hydrophobic interactions with the protein residues. Compound **26e** is shown as magenta sticks, and the protein residues involved in the interactions are rendered as cyan sticks. The hydrogen bonds are shown as black dashes, and interacting water molecules are shown as red spheres. (B) An overlay of DCAF1-**3d** and DCAF1-**26e** structures showing the location of the additional atoms in the **26e** compound and the binding site differences in the two proteins. Compounds and active site residues are rendered as described in Figure 3B and in panel A here.

high affinity DCAF1 antagonists by extending the molecule to the surface of the protein.

Antagonists that disrupt protein−protein interactions between DCAF1 and its interacting partners could be used toward development of therapeutics for cancers when DCAF1 is overexpressed,[26] and HIV when DCAF1 is hijacked by the virus.[15−17,23] In these cases, the small molecule prevents the binding of Vpr and Vpx to DCAF1, for example, preventing viral hijacking of the $CRL4^{DCAF1}$ or $EDVP^{DCAF1}$ complexes. Another potential application of antagonizing $CRL4^{DCAF1}$ function is in Merlin-deficient tumors. Merlin is a tumor suppressor that negatively regulates $CRL4^{DCAF1}$-mediated

https://doi.org/10.1021/acs.jmedchem.2c02132
J. Med. Chem. 2023, 66, 5041−5060

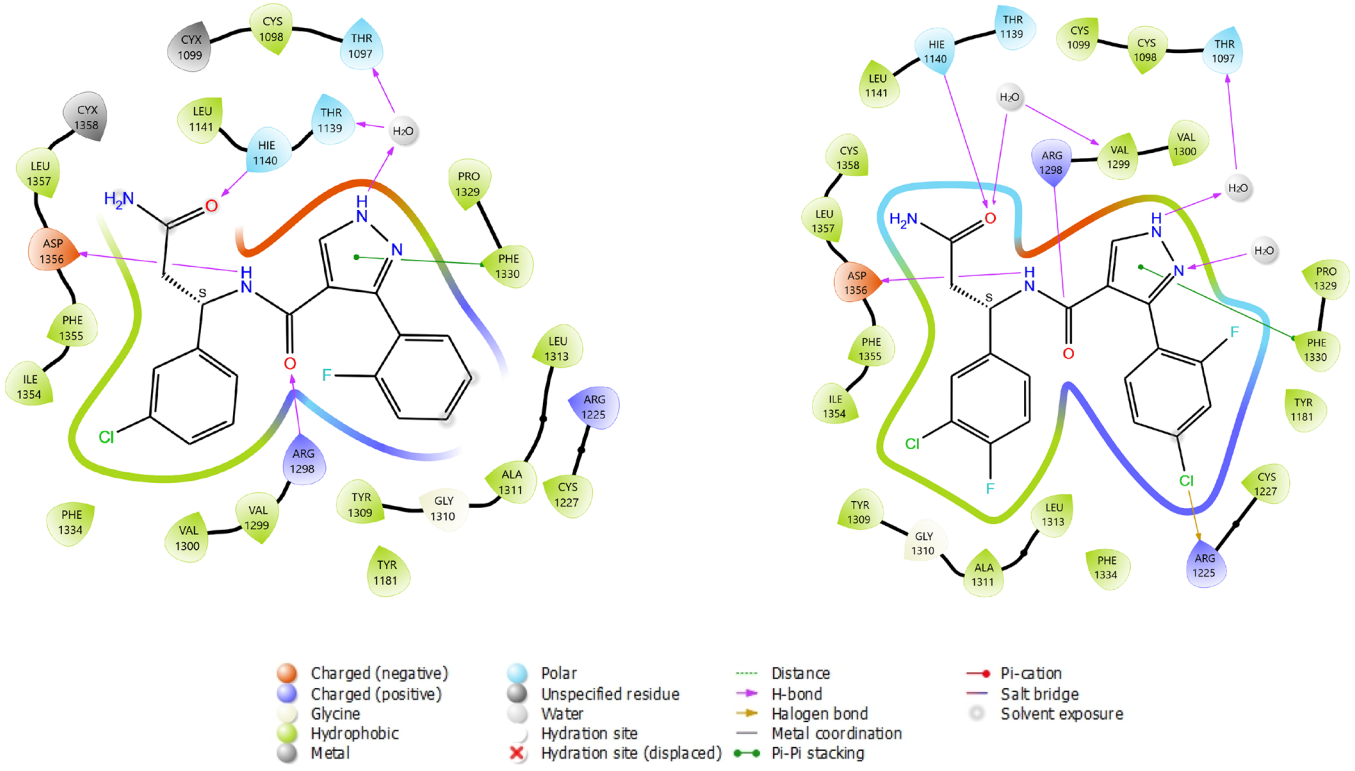

Figure 6. 2D interaction diagrams of **3d** and **26e** ligands in complex with DCAF1 protein. The most important interaction classes, including water-mediated hydrogen bonds, are represented. All protein residues within 5.0 Å from ligand are displayed. This picture has been generated using the LID tool from Maestro software (Schrodinger) from the prepared respective X-ray structures (7UFV and 8F8E).

ubiquitination of Lats1/2 in the Hippo pathway.[32] In Merlin-deficient tumorigenesis, $CRL4^{DCAF1}$-mediated ubiquitination is upregulated, and expression of Merlin or depletion of DCAF1 suppresses proliferation of tumor cells.[33,34] A DCAF1 antagonist can also function as a tool to discover novel biological functions of DCAF1.

CONCLUSIONS

We report the discovery of a novel series of small molecule ligands that target DCAF1. Specifically, **3d** and its more potent analog **26e** were identified using biophysical assays, showing binding to the DCAF1 WDR domain with K_d of 590 and 38 nM by SPR and K_d of 932 and 278 nM by ITC, respectively. Co-crystallization of **3d** in complex with the DCAF1 WDR domain allowed us to employ structure-guided SAR to optimize and develop **26e**. Interestingly, we also discovered that the S enantiomers of this chemical series were more potent than the R enantiomers. In addition to the biophysical characterization and co-crystallization of these compounds, we assessed the cellular target engagement and further confirmed that **26e** is binding to the DCAF1 WDR domain in cells with EC_{50} of 10.5 μM. Overall, we discovered a potent and in-cell active small molecule for the DCAF1 WDR domain along with the co-crystal structure of the DCAF1-**26e** complex that could guide the development of DCAF1 antagonists and DCAF1-based PROTACs as future cancer and viral therapeutics.

EXPERIMENTAL SECTION

Chemistry. All reagents were purchased from commercial vendors and used without further purification. Volatiles were removed under reduced pressure by rotary evaporation or by using the V-10 solvent evaporator system from Biotage. Very high boiling point (6000 rpm, 0 mbar, 56 °C), mixed volatile (7000 rpm, 30 mbar, 36 °C), and volatile (6000 rpm, 30 mbar, 36 °C) methods were used to evaporate solvents. The yields given refer to chromatographically purified and spectroscopically pure compounds, unless stated otherwise. Compounds were purified using either a Biotage Isolera One system or a Teledyne ISCO CombiFlash Rf system. Normal phase chromatography was performed using Biotage SNAP KP-Sil, Sfär Silica D (part no. FSKO-1107/FSRD-0445), Teledyne ISCO RediSep Rf silica (part no. 69-2203-3), or InnoFlash S series silica (part no. VI-1501) columns. Reverse-phase chromatography was performed using Biotage SNAP KP-C18-HS, Sfär C18 D (part no. FSLO-1118/FSUD-040) or Teledyne ISCO RediSep Rf C18 (part no. 69-2203-4) columns. Preparative chromatography was carried out using either a Waters 2767 injector with the collector attached to PDA UV/vis and SQD mass detectors or a Waters 3767 injector with the collector attached to PDA UV/vis and QDa mass detectors. An XSelect CSH Prep C18 5 μm OBD 19 × 100 mm (part no. 186005421) or Xselect CSH Prep C18 5 μm 10 × 100 mm (part no. 186005415) column was used for purification. Final compounds were dried using the Labconco Benchtop FreeZone Freeze-Dry System (4.5 L model). ^{1}H NMR spectra were recorded on a Bruker Avance-III 500 MHz spectrometer at ambient temperature. ^{13}C NMR spectra were recorded on an Agilent DD2 700 MHz spectrometer at ambient temperature. Residual protons of $CDCl_3$, DMSO-d_6, and CD_3OD solvents were used as internal references. Spectral data are reported as follows: chemical shift (δ in ppm), multiplicity (br = broad, s = singlet, d = doublet, dd = doublet of doublets, t = triplet, m = multiplet), coupling constants (J in Hz), and proton integration. Compound purity was determined by UV absorbance at 254 nm during tandem liquid chromatography/mass spectrometry (LCMS) using a Waters Acquity separations module. All final compounds had a purity of ≥95% as determined using this method. Low-resolution mass spectrometry was conducted in both positive and negative ion mode using a Waters Acquity SQD mass spectrometer (electrospray ionization source) fitted with a PDA detector. Mobile phase A consisted of 0.1% formic acid in water, whereas mobile phase B

https://doi.org/10.1021/acs.jmedchem.2c02132
J. Med. Chem. 2023, 66, 5041−5060

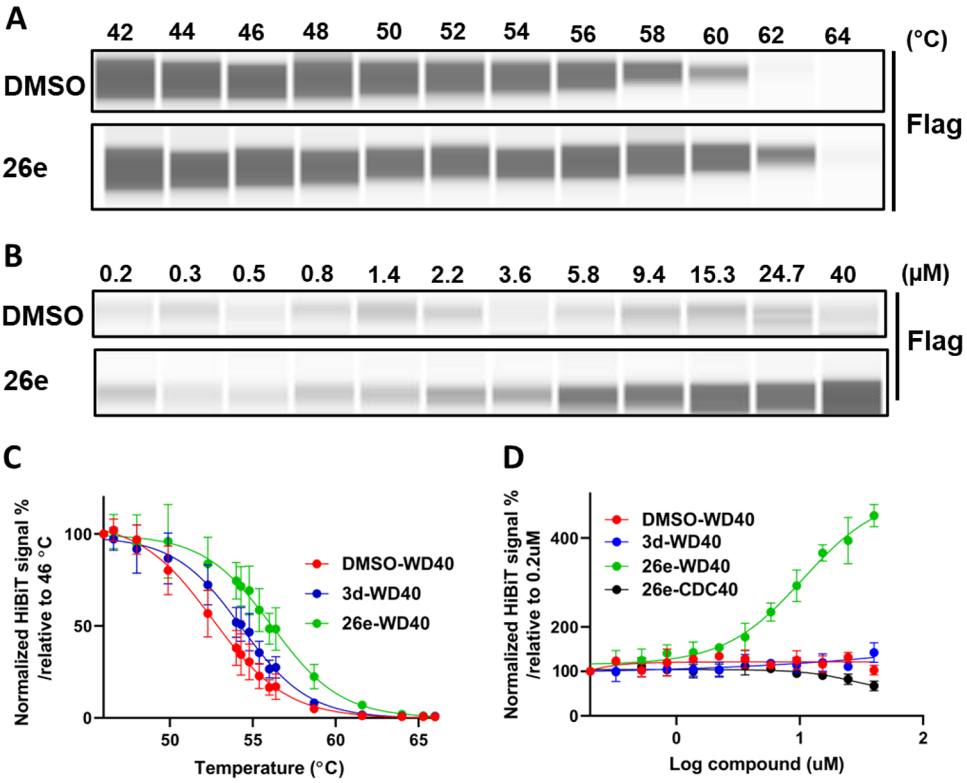

Figure 7. 26e engages the WDR domain of DCAF1 in cells. In a cellular thermal shift assay (CETSA) as described in the materials and methods, the amount of unaggregated flag tagged WDR domain of DCAF1 was quantified. (A) **26e** significantly stabilized the Flag-Hb-DCAF1-WD at 40 μM. (B) Titration of **26e** showed a dose-dependent pattern of DCAF1-WD stability. Different compound concentrations (40 to 0.2 μM) of **26e** were heated at 61 °C for 3.5 min. (C) When compared to the DMSO treatment, **26e** thermally stabilized the WDR domain of DCAF1 to a greater extent than **3d**, causing a 3.6 and 1.7 °C shift in the aggregation temperature of Flag-Hb-DCAF1_WD at 40 μM. Results shown as average ± SD (n = 3) (D) **26e** thermally stabilized Flag-Hb-DCAF1_WD in a dose-dependent manner with an EC_{50} value of 10.5 μM. Results shown as average ± SD (n = 3). CDC40 was used as a negative control. Note that in C, cells are subjected to a gradient of temperatures (46 to 66 °C). Across this range of temperatures, **3d** thermally stabilizes the WDR domain of DCAF1, but the stabilization does not extend beyond 61 °C. In D, the protein is kept at 61 °C, and consistent with our observation in C, **3d** was not expected to stabilize the WDR domain at any concentration.

consisted of 0.1% formic acid in acetonitrile. Analysis was carried out using an Acquity UPLC HSS T3 (2.1 × 50 mm, 100 Å, 1.8 μm. part no. 186003538) column. The gradient went from 98 to 5% mobile phase A over 1.8 min, maintained at 5% for 0.5 min, and then increased to 98% over 0.2 min for a total run time of 3 min. The flow rate was 0.4 mL/min, and all columns were used with the temperature maintained at 25 °C.

General Procedure A for the Synthesis of Compounds 3a, 3c−d, 14a−j, 15a−b, 15f, and 15j. A suspension of carboxylic acid **2** (0.27 mmol), amine **1** (0.24 mmol), and EDCI (0.27 mmol) in DCM (3 mL) was cooled to 0 °C in an ice bath. DIEA (0.54 mmol) was added, and the reaction was stirred at 0 °C for 5 min before the vial was removed from the ice bath and allowed to gradually warm to room temperature. After stirring at room temperature for 18 h, the reaction mixture was concentrated onto Celite under reduced pressure. Purification by flash chromatography on silica (2.5−10% MeOH in DCM with 0.5% NH_4OH), by reverse phase chromatography (5−60% MeCN in water with 0.1% formic acid), or by both if required afforded the products in 9−45% yield.

General Procedure B for the Synthesis of Compounds 5a−b. DIEA (0.22 mmol) and MsCl (0.22 mmol) were added to a stirring solution of carboxylic acid **4** (0.20 mmol) in DCM (2 mL) at 0 °C. After 10 min, an additional portion of DIEA (0.22 mmol) was added, and the solution of activated acid was transferred to a solution of amine **1** (0.20 mmol) in DCM (2 mL) also at 0 °C. After stirring for 30 min, the reaction was quenched with water, and the layers were separated. The aqueous layer was extracted with DCM, and the combined organics were dried and concentrated onto Celite. Purification by flash chromatography on silica (2.5−10% MeOH in DCM with 0.5% NH_4OH), by reverse phase chromatography (5−60% MeCN in water with 0.1% formic acid), or by both if required afforded the desired compounds in 5−70% yield.

General Procedure C for the Synthesis of Intermediates 12a−e. DIEA (1.6 mmol) was added to a suspension of β-amino acid **11** (1.4 mmol) and BOC_2O (1.6 mmol) in DCM (6 mL) at room temperature. After stirring for 18 h at room temperature, the volatiles were removed under reduced pressure. Purification by reverse phase chromatography (5−60% MeCN in water with 0.1% formic acid) afforded the desired intermediates in 33−78% yield.

General Procedure D for the Synthesis of Intermediates 13a−e. DIEA (2.8 mmol) was added to a stirring suspension of BOC protected β-amino acid **12** (0.57 mmol), NH_4Cl (1.7 mmol), and EDCI (0.68 mmol) in DCM (5 mL) at 0 °C. After 5 min, the reaction vial was removed from the ice bath and stirred at room temperature for 18 h. MeOH (0.5 mL) was added, and the reaction mixture was concentrated onto Celite under reduced pressure. Purification by flash chromatography (0.5−9.5% MeOH in DCM with 0.5% NH_4OH) afforded the desired intermediates in 19−49% yield.

General Procedure E for the Synthesis of Intermediates 1h−i and 1k−m. BOC protected β-amino amides **13** (0.18 mmol) were dissolved in 1,4-dioxane (2.0 mL) and treated with HCl (4.0 M in 1,4-dioxane) (2.0 mL, 4.0 mmol) at room temperature. After stirring at room temperature for 18 h, the reaction mixture was concentrated to dryness under reduced pressure to afford the desired intermediates in quantitative yield as their HCl salts that could be used without further purification.

General Procedure F for the Synthesis of Intermediates 17a−b. A mixture of benzaldehyde **16** (32 mmol), PPTS (1.6 mmol), (R)-2-methylpropane-2-sulfinamide (32 mmol), and $MgSO_4$ (158 mmol) in DCM (80 mL) was heated to 40 °C for 18 h. The

https://doi.org/10.1021/acs.jmedchem.2c02132
J. Med. Chem. 2023, 66, 5041−5060

reaction mixture was filtered through a pad of Celite, and the filtrate was concentrated to dryness under reduced pressure. Purification of the residue by flash chromatography on silica (10−20% EtOAc in hexanes) afforded the desired intermediates in 51−62% yield.

General Procedure G for the Synthesis of Intermediates 18a−b. A mixture of zinc powder (177 mmol) and copper(II) chloride (17.7 mmol) in THF (120 mL) was heated at reflux for 30 min under a nitrogen atmosphere. After cooling to room temperature, ethyl bromoacetate (44.2 mmol) in THF (10 mL) was added, and the reaction was heated at 50 °C for 30 min. The reaction was cooled to 0 °C, and intermediate **17** (17.7 mmol) in THF (20 mL) was added. The reaction was stirred for 2 h at 0 °C. The reaction mixture was filtered through a pad of Celite washing with EtOAc. The organic layer was washed with water and brine, dried over sodium sulfate, and concentrated to dryness under reduced pressure. Purification by flash chromatography on silica (40−60% EtOAc in hexanes) afforded the desired intermediates in 28−59% yield.

General Procedure H for the Synthesis of Intermediates 19a−b. A mixture of intermediate **18** (10.0 mmol) in 7 N methanolic ammonia (60 mL) was stirred for 5 h at room temperature. The reaction mixture was concentrated to dryness under reduced pressure. Purification by flash chromatography on silica (1−10% MeOH in DCM) afforded the desired intermediates in 66−93% yield.

General Procedure I for the Synthesis of Intermediates 1n−o. A mixture of intermediate **19** (3.3 mmol) and 4 N HCl in 1,4-dioxane (10 mL) was stirred at room temperature for 2 h. The reaction mixture was concentrated to dryness under reduced pressure. Trituration with Et_2O afforded the desired intermediates as powders in 49−64% yield.

General Procedure J for the Synthesis of Intermediates 23a−c. A mixture of intermediate **21** (2.15 mmol), boronic acid **22** (2.58 mmol), $Pd(PPh_3)_2Cl_2$ (0.215 mmol), and Cs_2CO_3 (4.72 mmol) in 1,4-dioxane (12 mL) and water (4 mL) under nitrogen was irradiated to 110 °C for 45 min. After cooling to room temperature, the reaction mixture was partitioned between DCM (100 mL) and water (50 mL), and the layers were separated. The aqueous layer was extracted with DCM (50 mL), and the combined organics were dried over sodium sulfate and concentrated to dryness. The residue was purified by flash chromatography on silica gel (0−25% EtOAc in hexanes) to afford the intermediates in 86−95% yield.

General Procedure K for the Synthesis of Intermediates 24a−c. A mixture of intermediate **23** (1.84 mmol) and KOH (5.51 mmol) in THF (6 mL), MeOH (2 mL), and water (6 mL) was heated to 70 °C for 3 h. After cooling to room temperature, the reaction mixture was partitioned between DCM (100 mL) and water (100 mL), and the layers were separated. The aqueous layer was acidified with 1 N HCl and extracted three times with DCM (50 mL). The combined organics were dried over magnesium sulfate and concentrated to dryness to afford the intermediates in 76−81% yield.

General Procedure L for the Synthesis of Intermediates 25a−e. DIEA (0.84 mmol) was added to a solution of intermediate **1** (0.84 mmol) and HATU (0.84 mmol) in DMF (4 mL) at room temperature. Intermediate **24** (0.70 mmol) was added, and the reaction was stirred at room temperature for 2 h and then at 45 °C for 18 h. The reaction mixture was concentrated to dryness under reduced pressure, and the residue was purified by flash chromatography on silica gel (40−100% EtOAc in hexanes) to afford the intermediates in >95% yield.

General Procedure M for the Synthesis of Compounds 26a−e. TFA (0.75 mL) was added to a solution of intermediate **25** (0.70 mmol) in DCM (4 mL) at room temperature. After stirring at room temperature for 2 h, the reaction mixture was neutralized with a 5% solution of NH_4OH in MeOH. The reaction mixture was concentrated to dryness under reduced pressure, and the residue was purified by preparative chromatography to afford the desired compounds 7−18% yield.

(*S*)-3-Amino-3-(2-fluorophenyl)propanamide Hydrochloride (1h). Quantitative yield; ESI-MS *m/z* 183.3 $[M + H]^+$.

(*S*)-3-Amino-3-(3-fluorophenyl)propanamide Hydrochloride (1i). Quantitative yield; ESI-MS *m/z* 183.0 $[M + H]^+$.

(*S*)-3-Amino-3-(2-methoxyphenyl)propanamide Hydrochloride (1k). Quantitative yield; ESI-MS *m/z* 195.4 $[M + H]^+$.

(*S*)-3-Amino-3-(3-methoxyphenyl)propanamide Hydrochloride (1l). Quantitative yield; ESI-MS *m/z* 195.3 $[M + H]^+$.

(*S*)-3-Amino-3-(4-methoxyphenyl)propanamide Hydrochloride (1m). Quantitative yield; ESI-MS *m/z* 195.4 $[M + H]^+$.

(*S*)-3-Amino-3-(3,4-dichlorophenyl)propanamide (1n). 64% yield; ESI-MS *m/z* 232.8 $[M + H]^+$.

(*S*)-3-Amino-3-(3-chloro-4-fluorophenyl)propanamide (1o). 49% yield; ESI-MS *m/z* 217.1 $[M + H]^+$.

(*R*)-*N*-(3-Amino-3-oxo-1-phenylpropyl)-3-phenyl-1*H*-pyrazole-4-carboxamide (3a). ^{1}H NMR (DMSO-d_6, 500 MHz) δ 13.39−13.12 (m, 1H), 8.47−8.39 (m, 1H), 8.21−7.92 (m, 1H), 7.73−7.62 (m, 2H), 7.42−7.28 (m, 8H), 7.26−7.20 (m, 1H), 6.83 (br s, 1H), 5.37 (q, *J* = 7.5 Hz, 1H), 2.59−2.56 (m, 2H); ESI-MS *m/z* 335.4 $[M + H]^+$; yield 28%; purity, 99.0%.

(*S*)-*N*-(3-Amino-3-oxo-1-phenylpropyl)-3-phenyl-1*H*-pyrazole-4-carboxamide (3b). ^{1}H NMR (DMSO-d_6, 500 MHz) δ 13.41−13.11 (m, 1H), 8.43 (br s, 1H), 8.21−7.92 (m, 1H), 7.73−7.62 (m, 2H), 7.44−7.28 (m, 8H), 7.25−7.20 (m, 1H), 6.83 (br s, 1H), 5.37 (q, *J* = 7.6 Hz, 1H), 2.59−2.56 (m, 2H); ESI-MS *m/z* 335.3 $[M + H]^+$; enamine; purity, 98.5%.

(*R*)-*N*-(3-Amino-1-(3-chlorophenyl)-3-oxopropyl)-3-(2-fluorophenyl)-1*H*-pyrazole-4-carboxamide (3c). ^{1}H NMR (DMSO-d_6, 500 MHz) δ 13.45−13.26 (m, 1H), 8.47−8.31 (m, 1H), 8.30−8.01 (m, 1H), 7.50−7.23 (m, 9H), 7.22−7.13 (m, 1H), 6.84 (br s, 1H), 5.31−5.25 (m, 1H), 2.57−2.55 (m, 2H); ESI-MS *m/z* 387.2 $[M + H]^+$; yield 38%; purity, 97.6%.

(*S*)-*N*-(3-Amino-1-(3-chlorophenyl)-3-oxopropyl)-3-(2-fluorophenyl)-1*H*-pyrazole-4-carboxamide (3d). ^{1}H NMR (DMSO-d_6, 500 MHz) δ 13.35 (br s, 1H), 8.37 (br s, 1H), 8.31−7.98 (m, 1H), 7.47−7.39 (m, 2H), 7.38−7.31 (m, 3H), 7.30−7.25 (m, 2H), 7.21 (br s, 2H), 6.84 (br s, 1H), 5.28 (q, *J* = 7.4 Hz, 1H), 2.58−2.55 (m, 2H); ESI-MS *m/z* 387.3 $[M + H]^+$; yield 24%; purity, 98.1%.

(*S*)-*N*-(3-Amino-1-(3-chlorophenyl)-3-oxopropyl)-1-methyl-3-phenyl-1*H*-pyrazole-4-carboxamide (5a). ^{1}H NMR (methanol-d_4, 500 MHz) δ 7.91 (d, *J* = 4.5 Hz, 1H), 7.48−7.44 (m, 2H), 7.28−7.22 (m, 4H), 7.22−7.13 (m, 3H), 5.36−5.30 (m, 1H), 3.84 (d, *J* = 4.6 Hz, 3H), 2.63−2.56 (m, 2H); ESI-MS *m/z* 383.3 $[M + H]^+$; yield 5%; purity, 95.1%.

(*S*)-*N*-(3-Amino-1-(3-chlorophenyl)-3-oxopropyl)-1-methyl-5-phenyl-1*H*-pyrazole-4-carboxamide (5b). ^{1}H NMR (DMSO-d_6, 500 MHz) δ 8.25 (d, *J* = 8.1 Hz, 1H), 7.99 (s, 1H), 7.48−7.44 (m, 3H), 7.41−7.38 (m, 2H), 7.34−7.29 (m, 3H), 7.28−7.25 (m, 1H), 7.23−7.21 (m, 1H), 6.83 (br s, 1H), 5.24 (q, *J* = 7.3 Hz, 1H), 3.65 (s, 3H), 2.54−2.52 (m, 2H); ESI-MS *m/z* 383.3 $[M + H]^+$; yield 70%; purity, 99.8%.

(*S*)-*N*-(3-(Methylamino)-3-oxo-1-phenylpropyl)-5-phenyl-1*H*-pyrazole-4-carboxamide (5c). To a solution of **10** (0.039 g, 0.077 mmol) in THF (1 mL) was added KOH (1.0 M in water) (1.0 mL, 1.0 mmol). The reaction was heated to 50 °C for 1 h. The reaction was cooled to room temperature and acidified with aqueous HCl (1.0 M in water) (∼1 mL). DCM (10 mL) and water (10 mL) were added, and the layers were separated. The aqueous layer was extracted with DCM (10 mL), and the combined organics were dried over sodium sulfate and concentrated to dryness to afford (*S*)-*N*-(3-(methylamino)-3-oxo-1-phenylpropyl)-5-phenyl-1*H*-pyrazole-4-carboxamide (0.025 g, 51%). ^{1}H NMR (DMSO-d_6, 500 MHz) δ 13.41−13.11 (m, 1H), 8.44 (br s, 1H), 8.19−7.90 (m, 1H), 7.78−7.74 (m, 1H), 7.72−7.62 (m, 2H), 7.40 (br s, 1H), 7.37−7.28 (m, 6H), 7.25−7.20 (m, 1H), 5.37 (q, *J* = 7.5 Hz, 1H), 3.30 (s, 3H), 2.60−2.57 (m, 2H); ESI-MS *m/z* 349.2 $[M + H]^+$; purity, 95.3%.

(*S*)-*N*-(1-(3-Chlorophenyl)-2-cyanoethyl)-3-(2-fluorophenyl)-1*H*-pyrazole-4-carboxamide (5d). TFAA (0.31 mL, 2.3 mmol) was added to a solution of **3d** (0.025 g, 0.065 mmol) in THF (1 mL) at room temperature. After stirring for 3 h, clean conversion to the nitrile along with TFA protection of the pyrazole was observed by UPLC-MS. The volatiles were removed under reduced pressure, and the residue was dissolved in MeOH (1 mL) and treated with K_2CO_3 (0.045 g, 0.32 mmol). After stirring for 18 h, the reaction mixture was concentrated onto Celite under reduced pressure and purified by

https://doi.org/10.1021/acs.jmedchem.2c02132
J. Med. Chem. 2023, 66, 5041−5060

reverse phase chromatography (5−60% MeCN in water with 0.1% formic acid) to afford (*S*)-*N*-(1-(3-chlorophenyl)-2-cyanoethyl)-3-(2-fluorophenyl)-1*H*-pyrazole-4-carboxamide (0.016 g, 67%). ^{1}H NMR (DMSO-d_6, 500 MHz) δ 13.34 (b s, 1H), 8.59 (b s, 1H), 8.36−7.95 (b m, 1H), 7.43−7.27 (m, 6H), 7.14 (b s, 2H), 5.26−5.19 (m, 1H), 3.04−2.90 (m, 2H); ESI-MS *m*/*z* 369.3 $[M + H]^+$; purity, 95.1%.

***tert*-Butyl (*S*)-(3-(methylamino)-3-oxo-1-phenylpropyl)-carbamate (7).** DIEA (0.16 mL, 0.94 mmol) was added to a solution of (*S*)-*N*-Boc-3-amino-3-phenylpropanoic acid (0.25 g, 0.94 mmol) and HATU (0.36 g, 0.94 mmol) in DMF (3 mL). After stirring for 15 min at room temperature, methylamine (2.0 M in THF) (1.4 mL, 2.8 mmol) was added, and the reaction was stirred at room temperature for 18 h. The reaction mixture was concentrated onto Celite under reduced pressure and purified by flash chromatography on silica gel (0.5−5.0% MeOH in DCM with 0.5% NH_4OH) to afford *tert*-butyl (*S*)-(3-(methylamino)-3-oxo-1-phenylpropyl)carbamate (0.24 g, 92%). ESI-MS *m*/*z* 279.4 $[M + H]^+$.

(*S*)-3-Amino-*N*-methyl-3-phenylpropanamide Hydrochloride (8). A solution of 7 (0.24 g, 0.87 mmol) was dissolved in 1,4-dioxane (5 mL) and treated with HCl (4.0 M in 1,4-dioxane) (0.94 mL, 3.8 mmol) at room temperature. After stirring for 1 h at room temperature, the reaction was concentrated to dryness under reduced pressure. Purification by reverse phase chromatography (0−50% MeCN in water with 0.1% formic acid) afforded (*S*)-3-amino-*N*-methyl-3-phenylpropanamide hydrochloride (0.18 g, 96%). ESI-MS *m*/*z* 179.3 $[M + H]^+$.

3-Phenyl-1-tosyl-1*H*-pyrazole-4-carboxylic Acid (9). A mixture of **2a** (0.075 g, 0.40 mmol) and TsCl (0.091 g, 0.48 mmol) in pyridine (2 mL) was allowed to stir at room temperature for 2 h. The reaction was concentrated to dryness and purified by flash chromatography on silica gel (0.5−9.5% MeOH in DCM) to afford 3-phenyl-1-tosyl-1*H*-pyrazole-4-carboxylic acid (0.048 g, 35%). ESI-MS *m*/*z* 343.2 $[M + H]^+$.

(*S*)-*N*-(3-(Methylamino)-3-oxo-1-phenylpropyl)-3-phenyl-1-tosyl-1*H*-pyrazole-4-carboxamide (10). DIEA (0.03 mL, 0.17 mmol) was added to a solution of **9** (0.048 g, 0.14 mmol) and HATU (0.064 g, 0.17 mmol) in DMF (1 mL) at room temperature. After stirring at room temperature for 15 min, this solution was added to a solution of (*S*)-3-amino-*N*-methyl-3-phenylpropanamide hydrochloride (0.036 g, 0.17 mmol) and DIEA (0.03 mL, 0.17 mmol) in DMF (1 mL) also at room temperature. After stirring for 18 h, the reaction mixture was concentrated onto Celite under reduced pressure and purified by flash chromatography on silica gel (0.5−9.5% MeOH in DCM with 0.5% NH_4OH) to afford (*S*)-*N*-(3-(methylamino)-3-oxo-1-phenylpropyl)-3-phenyl-1-tosyl-1*H*-pyrazole-4-carboxamide (0.039 g, 55%). ESI-MS *m*/*z* 503.3 $[M + H]^+$.

(*S*)-3-((*tert*-Butoxycarbonyl)amino)-3-(2-fluorophenyl)-propanoic Acid (12a). 67% yield; ESI-MS *m*/*z* 282.3 $[M - H]^-$.

(*S*)-3-((*tert*-Butoxycarbonyl)amino)-3-(3-fluorophenyl)-propanoic Acid (12b). 71% yield; ESI-MS *m*/*z* 282.4 $[M - H]^-$.

(*S*)-3-((*tert*-Butoxycarbonyl)amino)-3-(2-methoxyphenyl)-propanoic Acid (12c). 33% yield; ESI-MS *m*/*z* 294.4 $[M - H]^-$.

(*S*)-3-((*tert*-Butoxycarbonyl)amino)-3-(3-methoxyphenyl)-propanoic Acid (12d). 51% yield; ESI-MS *m*/*z* 294.4 $[M - H]^-$.

(*S*)-3-((*tert*-Butoxycarbonyl)amino)-3-(4-methoxyphenyl)-propanoic Acid (12e). 78% yield; ESI-MS *m*/*z* 294.4 $[M - H]^-$.

***tert*-Butyl (*S*)-(3-Amino-1-(2-fluorophenyl)-3-oxopropyl)-carbamate (13a).** 48% yield; ESI-MS *m*/*z* 283.4 $[M + H]^+$.

***tert*-Butyl (*S*)-(3-Amino-1-(3-fluorophenyl)-3-oxopropyl)-carbamate (13b).** 19% yield; ESI-MS *m*/*z* 283.2 $[M + H]^+$.

***tert*-Butyl (*S*)-(3-Amino-1-(2-methoxyphenyl)-3-oxopropyl)-carbamate (13c).** 42% yield; ESI-MS *m*/*z* 295.3 $[M + H]^+$.

***tert*-Butyl (*S*)-(3-Amino-1-(3-methoxyphenyl)-3-oxopropyl)-carbamate (13d).** 48% yield; ESI-MS *m*/*z* 295.2 $[M + H]^+$.

***tert*-Butyl (*S*)-(3-Amino-1-(4-methoxyphenyl)-3-oxopropyl)-carbamate (13e).** 49% yield; ESI-MS *m*/*z* 295.3 $[M + H]^+$.

***N*-(3-Amino-3-oxopropyl)-3-phenyl-1*H*-pyrazole-4-carboxamide (14a).** ^{1}H NMR (DMSO-d_6, 500 MHz) δ 13.37−13.07 (m, 1H), 8.16−7.86 (m, 2H), 7.80−7.66 (m, 2H), 7.47−7.31 (m, 4H), 6.82 (br s, 1H), 2.31 (t, *J* = 7.2 Hz, 2H), 1.29−1.24 (m, 2H); ESI-MS *m*/*z* 259.4 $[M + H]^+$; yield 45%; purity, 97.7%.

(*S*)-*N*-(3-Amino-1-(2-chlorophenyl)-3-oxopropyl)-3-phenyl-1*H*-pyrazole-4-carboxamide (14b). ^{1}H NMR (DMSO-d_6, 500 MHz) δ 13.41−13.05 (m, 1H), 8.42 (br s, 1H), 8.21−7.86 (m, 1H), 7.61 (br s, 2H), 7.41 (br d, *J* = 6.8 Hz, 1H), 7.36−7.17 (m, 8H), 6.83 (br s, 1H), 5.60−5.53 (m, 1H), 2.52−2.48 (m, 2H); ESI-MS *m*/*z* 369.3 $[M + H]^+$; yield 16%; purity, 95.3%.

(*S*)-*N*-(3-Amino-1-(3-chlorophenyl)-3-oxopropyl)-3-phenyl-1*H*-pyrazole-4-carboxamide (14c). ^{1}H NMR (DMSO-d_6, 500 MHz) δ 13.40−13.04 (m, 1H), 8.42 (br d, *J* = 8.1 Hz, 1H), 8.18−7.82 (m, 1H), 7.58 (br s, 2H), 7.35−7.19 (m, 8H), 6.79 (br s, 1H), 5.27 (q, *J* = 7.5 Hz, 1H), 2.53−2.50 (m, 2H); ESI-MS *m*/*z* 369.3 $[M + H]^+$; yield 12%; purity, 95.9%.

(*S*)-*N*-(3-Amino-1-(4-chlorophenyl)-3-oxopropyl)-3-phenyl-1*H*-pyrazole-4-carboxamide (14d). ^{1}H NMR (DMSO-d_6, 500 MHz) δ 13.35−13.05 (m, 1H), 8.40 (br d, *J* = 7.9 Hz, 1H), 8.16−7.83 (m, 1H), 7.59 (br s, 2H), 7.36−7.22 (m, 8H), 6.77 (br s, 1H), 5.26 (q, *J* = 7.5 Hz, 1H), 2.52−2.49 (m, 2H); ESI-MS *m*/*z* 369.3 $[M + H]^+$; yield 9%; purity, 95.9%.

(*S*)-*N*-(3-Amino-1-(2-fluorophenyl)-3-oxopropyl)-3-phenyl-1*H*-pyrazole-4-carboxamide (14e). ^{1}H NMR (DMSO-d_6, 500 MHz) δ 13.36−13.04 (m, 1H), 8.33 (br s, 1H), 8.15−7.84 (m, 1H), 7.65−7.54 (m, 2H), 7.39−7.17 (m, 6H), 7.12−7.03 (m, 2H), 6.78 (br s, 1H), 5.55−5.48 (m, 1H), 2.50−2.46 (m, 2H); ESI-MS *m*/*z* 353.5 $[M + H]^+$; yield 10%; purity, 98.0%.

(*S*)-*N*-(3-Amino-1-(3-fluorophenyl)-3-oxopropyl)-3-phenyl-1*H*-pyrazole-4-carboxamide (14f). ^{1}H NMR (DMSO-d_6, 500 MHz) δ 13.33−13.07 (m, 1H), 8.39 (br dd, *J* = 8.7, 11.4 Hz, 1H), 8.15−7.84 (m, 1H), 7.64−7.54 (m, 2H), 7.36−7.21 (m, 5H), 7.14−7.06 (m, 2H), 7.02−6.95 (m, 1H), 6.78 (br s, 1H), 5.30 (q, *J* = 7.6 Hz, 1H), 2.51 (br t, *J* = 6.6 Hz, 2H); ESI-MS *m*/*z* 353.3 $[M + H]^+$; yield 23%; purity, 95.1%.

(*S*)-*N*-(3-Amino-1-(4-fluorophenyl)-3-oxopropyl)-3-phenyl-1*H*-pyrazole-4-carboxamide (14g). ^{1}H NMR (DMSO-d_6, 500 MHz) δ 13.36−13.04 (m, 1H), 8.37 (br s, 1H), 8.13−7.83 (m, 1H), 7.65−7.55 (m, 2H), 7.37−7.21 (m, 6H), 7.06 (t, *J* = 8.9 Hz, 2H), 6.76 (br s, 1H), 5.28 (q, *J* = 7.6 Hz, 1H), 2.51−2.48 (m, 2H); ESI-MS *m*/*z* 353.4 $[M + H]^+$; yield 29%; purity, 98.2%.

(*S*)-*N*-(3-Amino-1-(2-methoxyphenyl)-3-oxopropyl)-3-phenyl-1*H*-pyrazole-4-carboxamide (14h). ^{1}H NMR (DMSO-d_6, 500 MHz) δ 13.33−13.07 (m, 1H), 8.18−7.84 (m, 2H), 7.65−7.56 (m, 2H), 7.37−7.22 (m, 3H), 7.21−7.08 (m, 3H), 6.89 (d, *J* = 8.1 Hz, 1H), 6.81 (t, *J* = 7.3 Hz, 1H), 6.74 (br s, 1H), 5.54−5.48 (m, 1H), 3.71 (s, 3H), 2.48−2.45 (m, 2H); ESI-MS *m*/*z* 365.2 $[M + H]^+$; yield 13%; purity, 95.7%.

(*S*)-*N*-(3-Amino-1-(3-methoxyphenyl)-3-oxopropyl)-3-phenyl-1*H*-pyrazole-4-carboxamide (14i). ^{1}H NMR (DMSO-d_6, 500 MHz) δ 13.33−13.05 (m, 1H), 8.33 (br dd, *J* = 8.4, 14.6 Hz, 1H), 8.11−7.84 (m, 1H), 7.66−7.56 (m, 2H), 7.36−7.21 (m, 4H), 7.15 (t, *J* = 7.8 Hz, 1H), 6.88−6.70 (m, 4H), 5.27 (q, *J* = 7.5 Hz, 1H), 3.66 (s, 3H), 2.50−2.47 (m, 2H); ESI-MS *m*/*z* 365.4 $[M + H]^+$; yield 16%; purity, 94.9%.

(*S*)-*N*-(3-Amino-1-(4-methoxyphenyl)-3-oxopropyl)-3-phenyl-1*H*-pyrazole-4-carboxamide (14j). ^{1}H NMR (DMSO-d_6, 500 MHz) δ 13.36−13.00 (m, 1H), 8.28 (br d, *J* = 8.2 Hz, 1H), 8.15−7.81 (m, 1H), 7.60 (br s, 2H), 7.37−7.17 (m, 6H), 6.82−6.77 (m, 2H), 6.72 (br s, 1H), 5.24 (q, *J* = 7.5 Hz, 1H), 3.65 (s, 3H), 2.49−2.46 (m, 2H); ESI-MS *m*/*z* 365.3 $[M + H]^+$; yield 33%; purity, 95.0%.

(*S*)-*N*-(3-Amino-3-oxo-1-phenylpropyl)-5-methyl-1*H*-pyrazole-4-carboxamide (15a). ^{1}H NMR (DMSO-d_6, 500 MHz) δ 12.81−12.59 (m, 1H), 8.22−7.81 (m, 2H), 7.32−7.20 (m, 5H), 7.17−7.11 (m, 1H), 6.75 (br s, 1H), 5.29 (q, *J* = 7.5 Hz, 1H), 2.52 (br d, *J* = 6.7 Hz, 2H), 2.32−2.21 (m, 3H); ESI-MS *m*/*z* 273.4 $[M + H]^+$; yield 28%; purity, 96.9%.

(*S*)-*N*-(3-Amino-3-oxo-1-phenylpropyl)-3-(2-chlorophenyl)-1*H*-pyrazole-4-carboxamide (15b). ^{1}H NMR (DMSO-d_6, 500 MHz) δ 13.22 (br s, 1H), 8.16 (br s, 2H), 7.45−7.17 (m, 9H), 7.13 (br d, *J* = 5.7 Hz, 1H), 6.72 (br s, 1H), 5.19 (q, *J* = 7.4 Hz, 1H), 2.47 (br d, *J* = 6.4 Hz, 2H); ESI-MS *m*/*z* 369.4 $[M + H]^+$; yield 20%; purity, 97.2%.

(*S*)-*N*-(3-Amino-3-oxo-1-phenylpropyl)-3-(3-chlorophenyl)-1*H*-pyrazole-4-carboxamide (15c). ^{1}H NMR (DMSO-d_6, 500

https://doi.org/10.1021/acs.jmedchem.2c02132
J. Med. Chem. 2023, 66, 5041−5060

MHz) δ 13.57−13.21 (m, 1H), 8.51 (br d, J = 8.2 Hz, 1H), 8.31−7.77 (m, 2H), 7.67 (br s, 1H), 7.44−7.28 (m, 7H), 7.25−7.20 (m, 1H), 6.83 (br s, 1H), 5.38 (q, J = 7.5 Hz, 1H), 2.59 (br d, J = 7.3 Hz, 2H); ESI-MS m/z 369.3 [M + H]+; Enamine; purity, 97.4%.

(*S*)-*N*-(3-Amino-3-oxo-1-phenylpropyl)-3-(4-chlorophenyl)-1*H*-pyrazole-4-carboxamide (15d). ^{1}H NMR (DMSO-d_6, 500 MHz) δ 13.50−13.21 (m, 1H), 8.53−8.46 (m, 1H), 8.28−7.95 (m, 1H), 7.80−7.45 (m, 3H), 7.41−7.29 (m, 6H), 7.26−7.20 (m, 1H), 6.84 (br s, 1H), 5.38 (q, J = 7.5 Hz, 1H), 2.58 (br d, J = 7.2 Hz, 2H); ESI-MS m/z 369.3 [M + H]+; Enamine; purity, 97.9%.

(*S*)-*N*-(3-Amino-3-oxo-1-phenylpropyl)-3-(2-fluorophenyl)-1*H*-pyrazole-4-carboxamide (15e). ^{1}H NMR (DMSO-d_6, 500 MHz) δ 13.43−13.22 (m, 1H), 8.44−8.00 (m, 2H), 7.43 (br s, 2H), 7.34−7.12 (m, 8H), 6.80 (br s, 1H), 5.30 (q, J = 7.3 Hz, 1H), 2.56 (br d, J = 6.8 Hz, 2H); ESI-MS m/z 353.5 [M + H]+; Enamine; purity, 99.7%.

(*S*)-*N*-(3-Amino-3-oxo-1-phenylpropyl)-3-(3-fluorophenyl)-1*H*-pyrazole-4-carboxamide (15f). ^{1}H NMR (DMSO-d_6, 500 MHz) δ 13.52−13.10 (m, 1H), 8.45 (br d, J = 7.7 Hz, 1H), 8.22−7.86 (m, 1H), 7.55−7.43 (m, 2H), 7.32−7.20 (m, 6H), 7.18−7.03 (m, 2H), 6.75 (br s, 1H), 5.30 (q, J = 7.5 Hz, 1H), 2.51 (br dd, J = 3.5, 6.8 Hz, 2H); ESI-MS m/z 353.2 [M + H]+; yield 26%; purity, 95.3%.

(*S*)-*N*-(3-Amino-3-oxo-1-phenylpropyl)-3-(4-fluorophenyl)-1*H*-pyrazole-4-carboxamide (15g). ^{1}H NMR (DMSO-d_6, 500 MHz) δ 13.44−13.12 (m, 1H), 8.45 (br d, J = 8.1 Hz, 1H), 8.26−7.92 (m, 1H), 7.75 (br s, 2H), 7.38−7.29 (m, 5H), 7.26−7.11 (m, 3H), 6.84 (br s, 1H), 5.37 (q, J = 7.5 Hz, 1H), 2.60−2.56 (m, 2H); ESI-MS m/z 353.3 [M + H]+; Enamine; purity, 97.5%.

(*S*)-*N*-(3-Amino-3-oxo-1-phenylpropyl)-3-(4-methoxyphenyl)-1*H*-pyrazole-4-carboxamide (15h. ^{1}H NMR (DMSO-d_6, 500 MHz) δ 13.27−13.03 (m, 1H), 8.41−8.34 (m, 1H), 8.18−7.88 (m, 1H), 7.69−7.59 (m, 2H), 7.38−7.28 (m, 5H), 7.25−7.19 (m, 1H), 7.00−6.81 (m, 3H), 5.36 (q, J = 7.6 Hz, 1H), 3.78 (br d, J = 10.0 Hz, 3H), 2.57 (br d, J = 6.8 Hz, 2H); ESI-MS m/z 365.4 [M + H]+; Enamine; purity, 97.8%.

(*S*)-*N*-(3-Amino-3-oxo-1-phenylpropyl)-3-(3-cyanophenyl)-1*H*-pyrazole-4-carboxamide (15i). ^{1}H NMR (DMSO-d_6, 500 MHz) δ 13.61−13.36 (m, 1H), 8.54 (br d, J = 7.8 Hz, 1H), 8.33−7.95 (m, 3H), 7.92−7.74 (m, 1H), 7.67−7.52 (m, 1H), 7.41−7.29 (m, 5H), 7.26−7.20 (m, 1H), 6.83 (br s, 1H), 5.39 (q, J = 7.6 Hz, 1H), 2.59 (br d, J = 7.2 Hz, 2H); ESI-MS m/z 360.5 [M + H]+; Enamine; purity, 95.1%.

(*S*)-*N*-(3-Amino-3-oxo-1-phenylpropyl)-3-(3-chloro-4-fluorophenyl)-1*H*-pyrazole-4-carboxamide (15j). ^{1}H NMR (DMSO-d_6, 500 MHz) δ 13.31 (br s, 1H), 8.45 (br d, J = 8.2 Hz, 1H), 8.25−8.02 (m, 1H), 7.91 (br d, J = 6.8 Hz, 1H), 7.83−7.61 (m, 1H), 7.42−7.20 (m, 6H), 7.18−7.13 (m, 1H), 6.76 (br s, 1H), 5.31 (q, J = 7.4 Hz, 1H), 2.51 (br d, J = 6.1 Hz, 2H); ESI-MS m/z 387.3 [M + H]+; yield 26%; purity, 96.0%.

(*R*,*E*)-*N*-(3,4-Dichlorobenzylidene)-2-methylpropane-2-sulfinamide (17a). 62% yield; ESI-MS m/z 278.1 [M + H]+.

(*R*,*E*)-*N*-(3-Chloro-4-fluorobenzylidene)-2-methylpropane-2-sulfinamide (17b). 51% yield; ESI-MS m/z 262.1 [M + H]+.

Ethyl (*S*)-3-(((*R*)-*tert*-Butylsulfinyl)amino)-3-(3,4-dichlorophenyl) Propanoate (18a). 28% yield; ESI-MS m/z 366.2 [M + H]+.

Ethyl (*S*)-3-(((*R*)-*tert*-Butylsulfinyl)amino)-3-(3-chloro-4-fluorophenyl) Propanoate (18b). 59% yield; ESI-MS m/z 350.2 [M + H]+.

(*S*)-3-(((*R*)-*tert*-Butylsulfinyl)amino)-3-(3,4-dichlorophenyl) Propanamide (19a). 66% yield; ESI-MS m/z 337.2 [M + H]+.

(*S*)-3-(((*R*)-*tert*-Butylsulfinyl)amino)-3-(3-chloro-4-fluorophenyl) Propanamide (19b). 93% yield; ESI-MS m/z 321.1 [M + H]+.

Ethyl 5-Bromo-1-((2-(trimethylsilyl)ethoxy)methyl)-1*H*-pyrazole-4-carboxylate (21). Ethyl 5-bromo-1*H*-pyrazole-4-carboxylate (5.0 g, 23 mmol) was added to a stirring suspension of sodium hydride (0.68 g, 28 mmol, 60% dispersion) in THF (40 mL) at 0 °C. After stirring for 45 min, (2-(chloromethoxy)ethyl)trimethylsilane (5.1 mL, 27 mmol) was added dropwise, and the solution was allowed to warm to room temperature. After stirring for 48 h, the reaction mixture was partitioned between DCM (200 mL) and water (100 mL), and the layers were separated. The aqueous layer was extracted with DCM (100 mL), and the combined organics were dried over sodium sulfate and concentrated to dryness. The residue was purified by flash chromatography on silica gel (0−25% EtOAc in hexanes) to afford ethyl 5-bromo-1-((2-(trimethylsilyl)ethoxy)methyl)-1*H*-pyrazole-4-carboxylate (5.3 g, 67%) as a mixture of regioisomers. ESI-MS m/z 349.1 [M + H]+.

Ethyl 5-(2-Fluorophenyl)-1-((2-(trimethylsilyl)ethoxy)methyl)-1*H*-pyrazole-4-carboxylate (23a). 95% yield; ESI-MS m/z 365.1 [M + H]+.

Ethyl 5-(2,4-Difluorophenyl)-1-((2-(trimethylsilyl)ethoxy)methyl)-1*H*-pyrazole-4-carboxylate (23b). 95% yield; ESI-MS m/z 383.3 [M + H]+.

Ethyl 5-(4-Chloro-2-fluorophenyl)-1-((2-(trimethylsilyl)ethoxy)methyl)-1*H*-pyrazole-4-carboxylate (23c). 86% yield; ESI-MS m/z 399.1 [M + H]+.

5-(2-Fluorophenyl)-1-((2-(trimethylsilyl)ethoxy)methyl)-1*H*-pyrazole-4-carboxylic Acid (24a). 81% yield; ESI-MS m/z 335.2 [M − H]−.

5-(2,4-Difluorophenyl)-1-((2-(trimethylsilyl)ethoxy)methyl)-1*H*-pyrazole-4-carboxylic Acid (24b). 79% yield; ESI-MS m/z 353.1 [M − H]−.

5-(4-Chloro-2-fluorophenyl)-1-((2-(trimethylsilyl)ethoxy)methyl)-1*H*-pyrazole-4-carboxylic Acid (24c). 76% yield; ESI-MS m/z 369.1 [M − H]−.

(*S*)-*N*-(3-Amino-1-(3-chloro-4-fluorophenyl)-3-oxopropyl)-5-(2-fluorophenyl)-1-((2-(trimethylsilyl)ethoxy)methyl)-1*H*-pyrazole-4-carboxamide (25a). 95% yield; ESI-MS m/z 535.1 [M + H]+.

(*S*)-*N*-(3-Amino-1-(3,4-dichlorophenyl)-3-oxopropyl)-5-(2-fluorophenyl)-1-((2-(trimethylsilyl)ethoxy)methyl)-1*H*-pyrazole-4-carboxamide (25b). 95% yield; ESI-MS m/z 551.3 [M + H]+.

(*S*)-*N*-(3-Amino-1-(3-chlorophenyl)-3-oxopropyl)-5-(2,4-difluorophenyl)-1-((2-(trimethylsilyl)ethoxy)methyl)-1*H*-pyrazole-4-carboxamide (25c). 95% yield; ESI-MS m/z 535.4 [M + H]+.

(*S*)-*N*-(3-Amino-1-(3-chlorophenyl)-3-oxopropyl)-5-(4-chloro-2-fluorophenyl)-1-((2-(trimethylsilyl)ethoxy)methyl)-1*H*-pyrazole-4-carboxamide (25d). 95% yield; ESI-MS m/z 551.2 [M + H]+.

(*S*)-*N*-(3-Amino-1-(3-chloro-4-fluorophenyl)-3-oxopropyl)-3-(4-chloro-2-fluorophenyl)-1-((2-(trimethylsilyl)ethoxy)methyl)-1*H*-pyrazole-4-carboxamide (25e). 95% yield; ESI-MS m/z 569.2 [M + H]+.

(*S*)-*N*-(3-Amino-1-(3-chloro-4-fluorophenyl)-3-oxopropyl)-5-(2-fluorophenyl)-1*H*-pyrazole-4-carboxamide (26a). ^{1}H NMR (DMSO-d_6, 500 MHz) δ 13.64−13.04 (m, 1H), 8.38 (br s, 1H), 8.14 (br s, 1H), 7.49 (dd, J = 2.0, 7.2 Hz, 1H), 7.47−7.40 (m, 2H), 7.38−7.28 (m, 3H), 7.26−7.16 (m, 2H), 6.85 (br s, 1H), 5.27 (q, J = 7.5 Hz, 1H), 2.57 (br dd, J = 1.9, 7.3 Hz, 2H); ESI-MS m/z 405.2 [M + H]+; yield 9%; purity, 96.2%.

(*S*)-*N*-(3-Amino-1-(3,4-dichlorophenyl)-3-oxopropyl)-5-(2-fluorophenyl)-1*H*-pyrazole-4-carboxamide (26b). ^{1}H NMR (DMSO-d_6, 500 MHz) δ 13.39−13.20 (m, 1H), 8.42−8.26 (m, 1H), 8.24−7.92 (m, 1H), 7.51−7.46 (m, 2H), 7.43−7.26 (m, 3H), 7.24−7.04 (m, 3H), 6.79 (br s, 1H), 5.21−5.15 (m, 1H), 2.49 (br d, J = 6.2 Hz, 2H); ESI-MS m/z 421.2 [M + H]+; yield 8%; purity, 95.1%.

(*S*)-*N*-(3-Amino-1-(3-chlorophenyl)-3-oxopropyl)-5-(2,4-difluorophenyl)-1*H*-pyrazole-4-carboxamide (26c). ^{1}H NMR (DMSO-d_6, 500 MHz) δ 13.32 (br s, 1H), 8.36−8.18 (m, 1H), 7.40 (br s, 1H), 7.29−7.23 (m, 3H), 7.22−7.18 (m, 2H), 7.05 (br s, 1H), 6.77 (br s, 1H), 5.21 (q, J = 7.4 Hz, 1H), 2.49 (br d, J = 7.3 Hz, 2H); ESI-MS m/z 405.2 [M + H]+; yield 7%; purity, 97.6%.

(*S*)-*N*-(3-Amino-1-(3-chlorophenyl)-3-oxopropyl)-5-(4-chloro-2-fluorophenyl)-1*H*-pyrazole-4-carboxamide (26d). ^{1}H NMR (DMSO-d_6, 500 MHz) δ 13.46−13.24 (m, 1H), 8.33 (br s, 1H), 8.27−7.94 (m, 1H), 7.38 (br s, 1H), 7.31−7.17 (m, 6H), 6.77 (br s, 1H), 5.21 (q, J = 7.5 Hz, 1H), 2.49 (br dd, J = 3.2, 7.3 Hz, 2H); ESI-MS m/z 421.2 [M + H]+; yield 8%; purity, 99.1%.

https://doi.org/10.1021/acs.jmedchem.2c02132
J. Med. Chem. 2023, 66, 5041−5060

(*S*)-*N*-(3-Amino-1-(3-chloro-4-fluorophenyl)-3-oxopropyl)-3-(4-chloro-2-fluorophenyl)-1*H*-pyrazole-4-carboxamide (26e). ^{1}H NMR (DMSO-d_6, 500 MHz) δ 13.54−13.30 (m, 1H), 8.40 (br s, 1H), 8.34−8.01 (m, 1H), 7.52−7.43 (m, 2H), 7.42−7.25 (m, 5H), 6.85 (br s, 1H), 5.27 (q, J = 7.5 Hz, 1H), 2.57 (br dd, J = 2.8, 7.2 Hz, 2H); ^{13}C NMR (DMSO-d_6, 176 MHz) δ ppm 171.6, 161.9, 160.0, 155.8, 141.4, 132.9, 130.8, 129.0, 127.8, 124.6, 119.4, 116.9, 116.3, 49.4, 42.0; ESI-MS m/z 439.3 $[M + H]^+$; yield 18%; purity, 98.8%.

DEL Screening and Compound Ordering. The affinity-mediated selections included a pool of 59 DNA-encoded libraries as described in Cuozzo et al.[28] Purified protein (3.8 μM) DCAF1 (1038−1400) containing an N-terminal His6-tag was incubated in a solution with DNA-encoded library (40 μM) for1 h in a volume of 60 μL in 1× selection buffer, which consisted of HEPES (20 mM), potassium acetate (134 mM), sodium acetate (8 mM), sodium chloride (4 M), magnesium acetate (0.8 mM), 0.02% Tween20, sheared salmon sperm DNA (1 mg/mL, Invitrogen AM9680), imidazole (5 mM), and TCEP (1 mM) at pH 7.2. An additional selection condition containing the target and 100 μM of the Vpx peptide, as a competitor to possible compounds binding in the peptide binding site, was run in parallel. The Vpx peptide was preincubated with the DCAF1 target in 1× selection buffer for 0.5 h prior to addition of the DNA-encoded library. An additional selection condition containing no target was run in parallel to evaluate matrix binders. For each selection condition (no target, target, or target with competitor), a separate ME200 tip (Phynexus) containing 5 μL of nickel affinity matrix was prewashed three times in 200 μL of fresh 1× selection buffer. The affinity matrix used was cOmplete His-Tag Purification Resin (Sigma 5893682001). Each selection was separately captured with 20 passages over the ME200 tip for a total of 0.5 h. The bound protein/library captured on the ME200tip was washed eight times with 200 μL of, fresh 1× selection buffer. Bound library members were eluted by incubating the ME200tip with 60 μL of 1× fresh selection buffer at 85 °C for 5 min. The solution from the heat elution was incubated with 20 passages over a fresh, prewashed ME200 tip containing 5 μL of nickel affinity matrix to remove any eluted protein. This selection process was run for a second time using the eluate of the first selection in place of the input DNA-encoded library and using no target, fresh target, or fresh target with Vpx peptide. The eluate of the second round of selection was PCR amplified and sequenced as described in Cuozzo et al.

Sequence data were parsed, error-containing sequences were disregarded, amplification duplicates were removed, and building block and chemical scheme encodings were decoded and reported along with associated calculated statistical parameters. Significantly enriched instances from two- and three-cycle libraries were called into groupings based on similar chemical features to obtain 98 families. Up to 10 instances (fully enumerated structure and possible truncates) per family were used to structure similarity search the commercially available EnamineReal space (720 million, downloaded in 2018) applying a 2D Tanimoto ≥0.4 distance cutoff to obtain a representative set of potentially purchasable compounds. Duplicate structures were removed, and up to two identified commercial compounds per family were further evaluated by inspection (chirality check that matches building block chirality and deprioritizing compounds that resembled low count instances) to arrive at 40 EnamineReal diverse compounds, which were requested for synthesis from Enamine (Kyiv, Ukraine). Thirty-three compounds were successfully prepared and were submitted for assay evaluation. The DNA-encoded library selection data were also processed, as described in McCloskey et al., to obtain DCAF1 binding RF and GCNN models, used to score commercial compounds from EnamineReal, MCULE, and enumerated virtual libraries to support hit finding and hit expansion SAR workflows.

Protein Expression and Purification Used in Biophysical Characterization. The DNA fragment encoding human DCAF1 residues 1038−1400 was amplified by PCR and subcloned into pFBOH-MHL (derivative of the pFBOH-LIC vector, SGC). The resulting plasmid was transformed into DH10Bac Competent *E. coli* (Invitrogen), and recombinant viral DNA bacmid was purified and followed by a recombinant baculovirus expression in *Sf9* insect cells. Cells were harvested and lysed. Protein was purified through a pre-equilibrated Hispur Ni-NTA resin (Thermo Scientific) column and by gel filtration on a Superdex200 26/600 using an ÄKTA PURE (GE Healthcare) pre-equilibrated with 20 mM Tris−HCl pH 8.0, 150 mM NaCl, 5% glycerol, and 2 mM 2-mercaptoethanol. The purity of the fractions was confirmed on SDS-PAGE gels, and the pure fractions were pooled, concentrated, and flash frozen. Proteins were stored at −80 °C.

Differential Scanning Fluorimetry Assay. DSF experiments were performed using a Roche LightCycler 480 II in sealed Axygen 384-well plates (PCR-384-LC480). Reactions (20 μL) contained 0.1 mg/mL DCAF1 (1038−1400 aa) in 100 mM Hepes pH 7.5 and 150 mM NaCl, and SYPRO Orange (5000× SYPRO Orange stock in DMSO, Invitrogen, Cat # S6650). Compounds were tested at 200 μM with a final concentration of 1% DMSO. The initial hit compound was serially diluted to a final concentration of 400 to 25 μM with a final concentration of 2% DMSO. Thermal denaturation was monitored from 20 to 95 °C at a rate of 4 °C increase per minute, and data points were collected at 0.5 °C intervals.

Surface Plasmon Resonance. SPR studies were performed using a Biacore T200 (GE Health Sciences Inc.) at 20 °C. Biotinylated DCAF1 (1038−1400 aa) was captured onto two flow cells of a streptavidin-conjugated SA chip (according to manufacturer's protocol) achieving 4000−7000 response units (RU), whereas another flow cell was left empty for reference subtraction. Biotinylated WDR5 was captured on another flow cell as a negative control protein. Compounds were dissolved in 100% DMSO (20 mM stock) and diluted to working concentrations in 100% DMSO before threefold serial dilutions prepared in buffer with DMSO. For SPR analysis, compounds were diluted in HBS-EP buffer (10 mM Hepes pH 7.4, 150 mM NaCl, 3 mM EDTA, 0.05% Tween-20), giving a final concentration of 0.5 or 1% DMSO. Kinetic determination experiments were performed using single cycle kinetics with an on time of 60 s, off time of 120 s, and flow rate of 75 μL/min. Kinetic curve fittings and K_d calculations were done with a 1:1 binding model and the Biacore T200 Evaluation software (GE Health Sciences Inc.).

Isothermal Titration Calorimetry. Purified DCAF1 was dialyzed and diluted in HBS-EP buffer. Compounds (0.5 mM) were injected into the sample cell containing 40 μM DCAF1 with 2.5% DMSO. ITC titrations were performed on a Nano ITC from TA Instruments (New Castle, DE) at 25 °C by using 2 μL injections with a total of 24 injections. The final DMSO concentration of the DCAF1 solution was adjusted to 2.5%. K_d values of compound **3d** were obtained from three independent experiments. Compound **26e** (0.2 mM) was injected into the sample cell containing 20 μM DCAF1 with 2.0% DMSO. ITC titrations were performed on an Affinity ITC from TA Instruments at 25 °C by using 2 μL injections with a total of 24 injections. The final DMSO concentration of the DCAF1 solution was adjusted to 2.0%. K_d values of compound **26e** were obtained from three independent experiments. Data were fitted with a one-binding-site model using the Nano Analyze software.

Molecular Modeling. *Analysis of X-ray Structure.* The analysis of X-ray structures was done using both Pymol and Maestro software from Schrodinger. Low energy conformations for ligands were generated using the LigPrep tool within the Maestro software. The Glide docking tool from Schrodinger was used for the docking simulations with default parameters.

Hit-to-Lead. The SeeSAR software from BioSolveIT was used in the hit-to-lead stage. It relies on the HYDE[35] scoring function to evaluate atom-based affinity contributions to the binding energy. This is particularly interesting to predict the impact (favorable, neutral, or detrimental) of a given modification. As a preliminary check, SeeSAR was successfully challenged to explain the main activity cliffs from the known SAR from a 3D point of view. Following this positive control stage, a systematic exploration of the chemical space around the compound series was performed from an *in silico* point of view. This was achieved by plugging in a dictionary of commonly used organic modifications (functional groups and decorated rings with varied spacer lengths) at varied positions of the compound series (ortho/

https://doi.org/10.1021/acs.jmedchem.2c02132
J. Med. Chem. 2023, 66, 5041−5060

meta/para-positions of both southern and northern rings, replacement of the side chain amide). The designed libraries were subsequently postprocessed to discard compounds with undesired substructures or with unreasonable physicochemical properties. Besides, proper microspecies and tautomers were also generated using LigPrep. Finally, a single 3D conformer was generated for each kept compound and superimposed onto the experimental binding mode of the reference compound **3d**. Finally, the designed compounds were directly evaluated in the SeeSAR software using the template-based docking mode (with compound **3d** as the reference ligand). Several parameters were used to prioritize the compounds to be synthesized (HYDE evaluation, visual inspection of predicted binding modes, quality of torsion angles, absence of inter/intra-clashes, and physicochemical properties such as logP).

Crystallization and Structure Determination. *DCAF1 WDR Domain Gene Cloning, Protein Expression, and Purification.* The WDR domain (residues 1077−1390) of the human DCAF1 gene (UniProtKB Q9Y4B6) was cloned into an in-house insect cell expression vector pFBOH-MHL containing an N-terminal His_6-tag followed by a TEV cleavage site. Site-directed mutagenesis was then carried out to change residues 1077 (Phe) and 1079 (Arg) to alanine. The resultant construct was used for protein expression in a baculovirus-*Sf9* expression system following an optimized protocol as described by Hutchinson and Seitova.[36] The cells were harvested by centrifugation, resuspended in a lysis buffer (50 mM Tris−HCl pH 7.5, 5% glycerol, 0.4 M NaCl, 0.1% NP40, protease inhibitor cocktail, and benzonase endonuclease), and lysed by sonication. The cell lysate was then centrifuged, and the supernatant was filtered prior to purification.

The filtered cell-free extract was preincubated with TALON immobilized cobalt affinity resin equilibrated with the binding buffer containing 50 mM Tris−HCl pH 7.5, 5% glycerol, and 0.4 M NaCl prior to loading onto an open column. The column was washed with binding buffer and then with the same buffer containing 5 and 10 mM imidazole before elution with a buffer containing 250 mM imidazole. The eluted protein was then dialyzed overnight into 50 mM Tris−HCl pH 7.5, 0.4 M NaCl, 5% glycerol, and 10 mM β-mercaptoethanol in the presence of TEV protease to remove the polyhistidine (His_6) tag. The following day, the dialyzed protein was passed through the TALON cobalt affinity resin in an open column, and the flow-through (cleaved protein) was collected.

The collected protein sample was further purified by size exclusion chromatography using a HiLoad 26/600 Superdex 200 column (GE Healthcare) on an AKTA Pure chromatography system (GE Healthcare) with a running buffer containing 20 mM Tris−HCl pH 7.5, 150 mM NaCl, and 1 mM TCEP. The protein purity was assessed on an SDS-PAGE gel, and the pure peak fractions were then pooled and concentrated using 10 kDa cutoff centrifugal filters (Millipore). The protein concentration was determined using Nanodrop (Thermo Scientific) and calculated using the DCAF1 WDR protein extinction coefficient of 35,410 M^{-1} cm^{-1} (calculated from the amino acid sequence using Expasy ProtParam (https://web.expasy.org/protparam/)). The concentrated protein was then flash-frozen in liquid nitrogen before storage at −80 °C.

Protein Crystallization. We first attempted to co-crystallize the longer DCAF1 WDR domain construct (1061−1399 residues) as reported in the deposited APO structure (PDB ID: 4PXW), but crystallization was not reproducible. Also, the N-terminal region outside the WDR ring was not visible in the apo structure, so we considered designing a shorter construct for crystallization trials covering the WDR domain only, which generated robust and well-diffracting crystals. To generate DCAF1-**3d** and DCAF1-**26e** co-crystals, the protein (in 20 mM Tris−HCl pH 7.5, 150 mM NaCl, and 1 mM TCEP) at 10 mg/mL (0.2812 mM) was preincubated at room temperature with 4.218 mM (15 times molar excess) **3d** and **26e** compounds prior to crystallization. Crystallization screenings were performed using a Phenix drop dispensing robot (Art Robbins) with 0.5 μL of protein−compound solution and 0.5 μL of screen solution over a 90 μL reservoir in 96-well vapor diffusion sitting-drop plates. Diamond-shaped crystals were obtained after 72 h at 18 °C in a precipitant solution containing 20% PEG3350 and 0.2 M potassium fluoride for the DCAF1-**3d** and 20% PEG3350 and 0.2 M di-ammonium citrate for the DCAF1-**26e**.

Diffraction Data Collection, Structure Determination, and Refinement. Crystals were mounted in a nylon loop and cryoprotected in the reservoir solution supplemented with 10% ethylene glycol and 2 mM compound before flash-freezing in liquid nitrogen. Diffraction data were collected on beamline 24-ID-C at the Advanced Photon Source in Argonne National Laboratory. For the DCAF1-**3d**, the images were processed using XDS[37] and Aimless,[38] and the structure was phased by molecular replacement using Phaser[39] and the DCAF1 apo crystal structure (PDB ID: 4PXW) as a starting model. On the other hand, the DCAF1-**26e** images were processed using HKL3000,[40] and the structure was phased by molecular replacement using the DCAF1-**3d** (PDB: 7UFV) as a starting model. Following molecular replacement, the structures were refined using iterative cycles of manual model building in Coot[41] and refinement in REFMAC5[42] within the CCP4 crystallography suite.[43] The PDB and CIF files of the **3d** and **26e** compounds were generated using the Grades global phasing server (http://grade.globalphasing.org/cgi-bin/grade/server.cgi). Model validation was performed using the Molprobity[44] server, the structures were analyzed using PoseView[45] and UCSF Chimera,[46] and the graphical images were rendered using PyMOL.[47] The structural data for DCAF1-**3d** and DCAF1-**26e** were deposited in the Protein Data Bank (PDB) under the accession codes 7UFV and 8F8E, respectively.

Generation of HiBiT-DCAF1 NCI-H460 Cells. The WD40 domain (1038-1400aa) of DCAF1 with N-terminal 3x-flag and HiBiT tags (Flag-Hb-DCAF1_WD) was synthesized and inserted into the pDONR221 plasmid by GeneArt (Invitrogen). The construct was cloned into a pLV series lentiviral transfer plasmid containing a CMV promoter for expression and blasticidin selectable marker. Lentivirus infections were performed by treating one well of a six-well plate containing 100,000 parental NCI-H460 cells (ATCC) with 20 μL of concentrated virus followed by 2 days of incubation (37 °C, 5% CO_2) without removing the virus. The viral medium was replaced with fresh medium containing Blasticidin (InvivoGen; ANT-BL-1) to select and generate NCI-H460 cell lines stably expressing Flag-Hb-DCAF1_WD. The expression of the WD40 domain was confirmed via western blot. NCI-H460 cells stably expressing the full-length DCAF1 (Flag-Hb-DCAF1_FL) were also generated.

HiBit-DCAF1 Cellular Thermal Shift Assay (CETSA). NCI-H460 cells expressing Flag-Hb-DCAF1_WD or Flag-Hb-DCAF1_FL were seeded at 10,000 cells/50 μL (RPMI+10% FBS) per well of a 96-well black PCR plate. For the thermal shift assay, HP D300e digital dispenser was used to spray DMSO and 40 μM of **26e** or **3d**, and the plate was mixed using an orbital shaker for 15 s. Cells were incubated at 37 °C and 5% CO_2 for 1 h and then heated for 3.5 min at different temperatures using C1000 Touch Thermal Cycler (Bio-Rad; 1851196). For the CETSA dose−response assay, an HP D300e digital dispenser sprayed 12 different compound concentrations (40 to 0.2 μM) of **26e** or **3d** onto cells that were heated at one fixed 61 °C temperature for 3.5 min. An equal volume of NanoGlo HiBiT Lytic (Promega), containing both LgBiT protein and furimazine substrate, was added to the cells. Together, the HiBiT and the LgBiT protein formed a luminescent nanoluciferase enzyme, which emits light in the presence of the furimazine substrate. The luminesce signal is proportional to the unaggregated HiBiT tagged protein. The plate was mixed on an orbital shaker (500 rpm) for 10 min, and a Cytation 3 (BioTek) plate reader measured the emitted luminescence signal.

Quantitative Protein Expression Using Jess (ProteinSimple) to Detect Unaggregated Protein. One million cells/100 μL (RPMI + 10% FBS) of NCI-H460 cells expressing the HiBiT-tagged protein of interest were seeded per well of a 96-well TC plate. For thermal shift assay, an HP D300e digital dispenser sprayed DMSO or 40 μM of **26e**, and the plate was mixed using an orbital shaker for 15 s. Cells were incubated at 37 °C and 5% CO_2 for 1 h. Cells were then transferred to 1.5 mL Eppendorf tubes and spun at 500*g* for 5 min. The medium was aspirated, and cells were resuspended in a 100 μL of PBS with protease inhibitor. Cells were then transferred to PCR strip

https://doi.org/10.1021/acs.jmedchem.2c02132
J. Med. Chem. 2023, 66, 5041−5060

tubes and heated for 3.5 min at 12 different temperatures (42 to 64 °C with increments of 2 °C) using a Veriti 96-Well Fast Thermal Cycler (Applied Biosystems; 9902). Liquid nitrogen was used to freeze−thaw the cells twice, and then the cell lysate was centrifuged at 20,000*g* for 20 min at 4 °C. The supernatant with the unaggregated soluble protein was transferred into new 1.5 mL Eppendorf tubes. For the CETSA dose−response assay, the HP D300e digital dispenser sprayed DMSO or 12 different compound concentrations (40 to 0.2 μM) of **26e**. Cells were then heated at one fixed 61 °C temperature. The Jess (ProteinSimple; JS-4296), which automates traditional western blot, was used to detect and quantify the N-flag tagged DCAF1 WD40 domain.

■ ASSOCIATED CONTENT

Supporting Information

The Supporting Information is available free of charge at https://pubs.acs.org/doi/10.1021/acs.jmedchem.2c02132.

DSF amenability for DCAF1; ITC data for Z1391232269; crystallographic data for compounds **3d** and **26e**; CETSA data for full-length DCAF1; DSF data for compound **26e**; and NMR and LCMS spectral data for tested compounds (PDF)

Molecular formula strings (CSV)

■ AUTHOR INFORMATION

Corresponding Authors

Peter J. Brown − *Structural Genomics Consortium, University of Toronto, Toronto, Ontario M5G 1L7, Canada;* orcid.org/0000-0002-8454-0367; Email: peterj.brown@utoronto.ca

Levon Halabelian − *Structural Genomics Consortium, University of Toronto, Toronto, Ontario M5G 1L7, Canada; Department of Pharmacology and Toxicology, University of Toronto, Toronto, Ontario M5S 1A8, Canada;* orcid.org/0000-0003-4361-3619; Email: l.halabelian@utoronto.ca

Rima Al-awar − *Drug Discovery Program, Ontario Institute for Cancer Research, Toronto, Ontario M5G 0A3, Canada; Department of Pharmacology and Toxicology, University of Toronto, Toronto, Ontario M5S 1A8, Canada; Department of Chemistry, University of Toronto, Toronto, Ontario M5S 3H6, Canada*; Email: Rima.alawar@oicr.on.ca

Masoud Vedadi − *Structural Genomics Consortium, University of Toronto, Toronto, Ontario M5G 1L7, Canada; Drug Discovery Program, Ontario Institute for Cancer Research, Toronto, Ontario M5G 0A3, Canada; Department of Pharmacology and Toxicology, University of Toronto, Toronto, Ontario M5S 1A8, Canada;* orcid.org/0000-0002-0574-0169; Phone: 416-432-1980; Email: m.vedadi@utoronto.ca, mvedadi@oicr.on.ca

Authors

Alice Shi Ming Li − *Structural Genomics Consortium, University of Toronto, Toronto, Ontario M5G 1L7, Canada; Drug Discovery Program, Ontario Institute for Cancer Research, Toronto, Ontario M5G 0A3, Canada; Department of Pharmacology and Toxicology, University of Toronto, Toronto, Ontario M5S 1A8, Canada;* orcid.org/0000-0003-1093-9698

Serah Kimani − *Structural Genomics Consortium, University of Toronto, Toronto, Ontario M5G 1L7, Canada; Princess Margaret Cancer Centre, University Health Network, Toronto, Ontario M5G 2C1, Canada*

Brian Wilson − *Drug Discovery Program, Ontario Institute for Cancer Research, Toronto, Ontario M5G 0A3, Canada*

Mahmoud Noureldin − *Drug Discovery Program, Ontario Institute for Cancer Research, Toronto, Ontario M5G 0A3, Canada; Department of Pharmacology and Toxicology, University of Toronto, Toronto, Ontario M5S 1A8, Canada*

Héctor González-Álvarez − *Drug Discovery Program, Ontario Institute for Cancer Research, Toronto, Ontario M5G 0A3, Canada; Department of Pharmacology and Toxicology, University of Toronto, Toronto, Ontario M5S 1A8, Canada*

Ahmed Mamai − *Drug Discovery Program, Ontario Institute for Cancer Research, Toronto, Ontario M5G 0A3, Canada*

Laurent Hoffer − *Drug Discovery Program, Ontario Institute for Cancer Research, Toronto, Ontario M5G 0A3, Canada*

John P. Guilinger − *X-Chem Inc., Waltham, Massachusetts 02453, United States*

Ying Zhang − *X-Chem Inc., Waltham, Massachusetts 02453, United States*

Moritz von Rechenberg − *Relay Therapeutics, Cambridge, Massachusetts 02139, United States*

Jeremy S. Disch − *Relay Therapeutics, Cambridge, Massachusetts 02139, United States;* orcid.org/0000-0002-0357-1672

Christopher J. Mulhern − *Relay Therapeutics, Cambridge, Massachusetts 02139, United States*

Belinda L. Slakman − *Relay Therapeutics, Cambridge, Massachusetts 02139, United States*

John W. Cuozzo − *Relay Therapeutics, Cambridge, Massachusetts 02139, United States;* orcid.org/0000-0002-6229-0395

Aiping Dong − *Structural Genomics Consortium, University of Toronto, Toronto, Ontario M5G 1L7, Canada*

Gennady Poda − *Drug Discovery Program, Ontario Institute for Cancer Research, Toronto, Ontario M5G 0A3, Canada; Leslie Dan Faculty of Pharmacy, University of Toronto, Toronto, Ontario M5S 3M2, Canada*

Mohammed Mohammed − *Drug Discovery Program, Ontario Institute for Cancer Research, Toronto, Ontario M5G 0A3, Canada*

Punit Saraon − *Drug Discovery Program, Ontario Institute for Cancer Research, Toronto, Ontario M5G 0A3, Canada*

Manish Mittal − *Piramal Discovery Solutions, Pharmaceutical Special Economic Zone, Ahmedabad, Gujarat 382213, India*

Pratik Modh − *Piramal Discovery Solutions, Pharmaceutical Special Economic Zone, Ahmedabad, Gujarat 382213, India*

Vaibhavi Rathod − *Piramal Discovery Solutions, Pharmaceutical Special Economic Zone, Ahmedabad, Gujarat 382213, India*

Bhashant Patel − *Piramal Discovery Solutions, Pharmaceutical Special Economic Zone, Ahmedabad, Gujarat 382213, India*

Suzanne Ackloo − *Structural Genomics Consortium, University of Toronto, Toronto, Ontario M5G 1L7, Canada*

Vijayaratnam Santhakumar − *Structural Genomics Consortium, University of Toronto, Toronto, Ontario M5G 1L7, Canada;* orcid.org/0000-0002-7001-557X

Magdalena M Szewczyk − *Structural Genomics Consortium, University of Toronto, Toronto, Ontario M5G 1L7, Canada*

Dalia Barsyte-Lovejoy − *Structural Genomics Consortium, University of Toronto, Toronto, Ontario M5G 1L7, Canada; Department of Pharmacology and Toxicology, University of Toronto, Toronto, Ontario M5S 1A8, Canada*

Cheryl H. Arrowsmith − *Structural Genomics Consortium and Department of Medical Biophysics, University of Toronto, Toronto, Ontario M5G 1L7, Canada; Princess*

Margaret Cancer Centre, University Health Network, Toronto, Ontario M5G 2C1, Canada; orcid.org/0000-0002-4971-3250

Richard Marcellus − *Drug Discovery Program, Ontario Institute for Cancer Research, Toronto, Ontario M5G 0A3, Canada*

Marie-Aude Guié − *X-Chem Inc., Waltham, Massachusetts 02453, United States*

Anthony D. Keefe − *X-Chem Inc., Waltham, Massachusetts 02453, United States*

Complete contact information is available at: https://pubs.acs.org/10.1021/acs.jmedchem.2c02132

Author Contributions

[&]A.S.M.L., S.K., and B.W. contributed equally.

Notes

The authors declare the following competing financial interest(s): J.P.G, Y.Z., M.A.G., A.D.K. are employees of X-Chem. M.v.R., J.S.D, B.L.S. and J.W.C. are or were (C.J.M.) employees of Relay Therapeutics and were employees of X-Chem at the time of writing. Employees and past employees may hold stocks and shares. All other authors declare no conflict of interest.

J.P.G, Y.Z., M.A.G., and A.D.K. are employees of X-Chem. M.v.R., J.S.D., B.L.S., and J.W.C. are or were (C.J.M.) employees of Relay Therapeutics and were employees of X-Chem at the time of writing. Employees and past employees may hold stocks and shares.

Authors will release the atomic coordinates upon article publication.

■ ACKNOWLEDGMENTS

We would like to thank Yanjun Li, Peter Loppnau, Almagul Seitova, Ashley Hutchinson, Pegah Ghiabi, and Taraneh Hajian for gene cloning, protein expression, and purification; Yelena Arnautova for X-ray structure evaluation and computational modeling; Antoine Dumas for structure enumeration; Surayya Sana for compound logistics; Enamine and MCULE for compound synthesis; and Google Accelerated Science for GCNN modeling. We acknowledge the Northeastern Collaborative Access Team beamlines, which are funded by the National Institute of General Medical Sciences from the National Institutes of Health (P30 GM124165). This research used resources of the Advanced Photon Source, a U.S. Department of Energy (DOE) Office of Science User Facility operated for the DOE Office of Science by Argonne National Laboratory under Contract No. DE-AC02-06CH11357. Structural Genomics Consortium is a registered charity (no: 1097737) that receives funds from Bayer AG, Boehringer Ingelheim, Bristol Myers Squibb, Genentech, Genome Canada through Ontario Genomics Institute [OGI-196], EU/EFPIA/OICR/McGill/KTH/Diamond Innovative Medicines Initiative 2 Joint Undertaking [EUbOPEN grant 875510], Janssen, Merck KGaA (aka EMD in Canada and US), Pfizer, and Takeda. Funding for the Ontario Institute for Cancer Research is provided by the Government of Ontario. Héctor González-Álvarez received a scholarship from the Mexican National Council on Science and Technology (CONACyT).

■ ABBREVIATIONS

BRD4, bromodomain-containing protein 4; CDC40, cell division cycle 40; CETSA, cellular thermal shift assay; CRBN, cereblon; CRL, cullin-RING ligase; CUL, cullin; DCAF, DDB1-Cul4-associated factor; DDB1, DNA damage binding protein 1; DEL, DNA-encoded library; DIEA, *N*,*N*-diisopropylethylamine; DSF, differential scanning fluorimetry; EDCI, 1-ethyl-3-(3-dimethylaminopropyl)carbodiimide; EDVP, EED-DDB1-VprBP; FKBP12, 12 kDa FK506-binding protein; HATU, hexafluorophosphate azabenzotriazole tetramethyl uronium; HECT, homologous to the E6-AP carboxyl terminus; ITC, isothermal titration calorimetry; K_D, dissociation constant; Lats, large tumor suppressor kinase; LID, ligand interaction diagram; PROTACs, proteolysis targeting chimeras; RBR, ring between ring finger; RING, really interesting new gene; SAMHD1, sterile alpha-motif and histidine-aspartate domain-containing protein 1; SD, standard deviation; SPR, surface plasmon resonance; T_m, melting temperature; UNG2, uracil DNA glycosylase 2; VHL, von Hippel−Lindau; Vpr, viral protein R; Vpx, viral protein X; WDR, WD repeat

■ REFERENCES

(1) Khan, S.; He, Y.; Zhang, X.; Yuan, Y.; Pu, S.; Kong, Q.; Zheng, G.; Zhou, D. PROteolysis TArgeting Chimeras (PROTACs) as emerging anticancer therapeutics. *Oncogene* **2020**, *39*, 4909−4924.

(2) Nalawansha, D. A.; Crews, C. M. PROTACs: An Emerging Therapeutic Modality in Precision Medicine. *Cell Chem. Biol.* **2020**, *27*, 998−1014.

(3) Zheng, N.; Shabek, N. Ubiquitin Ligases: Structure, Function, and Regulation. *Annu. Rev. Biochem.* **2017**, *86*, 129−157.

(4) Zou, Y.; Ma, D.; Wang, Y. The PROTAC technology in drug development. *Cell Biochem. Funct.* **2019**, *37*, 21−30.

(5) Ishida, T.; Ciulli, A. E3 Ligase Ligands for PROTACs: How They Were Found and How to Discover New Ones. *SLAS Discovery* **2021**, *26*, 484−502.

(6) Baek, K.; Scott, D. C.; Schulman, B. A. NEDD8 and ubiquitin ligation by cullin-RING E3 ligases. *Curr. Opin. Struct. Biol.* **2021**, *67*, 101−109.

(7) Zhou, Z.; Song, X.; Wavelet, C. M.; Wan, Y. Cullin 4-DCAF Proteins in Tumorigenesis. *Adv. Exp. Med. Biol.* **2020**, *1217*, 241−259.

(8) Fischer, E. S.; Böhm, K.; Lydeard, J. R.; Yang, H.; Stadler, M. B.; Cavadini, S.; Nagel, J.; Serluca, F.; Acker, V.; Lingaraju, G. M.; Tichkule, R. B.; Schebesta, M.; Forrester, W. C.; Schirle, M.; Hassiepen, U.; Ottl, J.; Hild, M.; Beckwith, R. E. J.; Harper, J. W.; Jenkins, J. L.; Thomä, N. H. Structure of the DDB1-CRBN E3 ubiquitin ligase in complex with thalidomide. *Nature* **2014**, *512*, 49−53.

(9) Angers, S.; Li, T.; Yi, X.; MacCoss, M. J.; Moon, R. T.; Zheng, N. Molecular architecture and assembly of the DDB1-CUL4A ubiquitin ligase machinery. *Nature* **2006**, *443*, 590−593.

(10) Jin, J.; Arias, E. E.; Chen, J.; Harper, J. W.; Walter, J. C. A family of diverse Cul4-Ddb1-interacting proteins includes Cdt2, which is required for S phase destruction of the replication factor Cdt1. *Mol. Cell* **2006**, *23*, 709−721.

(11) He, Y. J.; McCall, C. M.; Hu, J.; Zeng, Y.; Xiong, Y. DDB1 functions as a linker to recruit receptor WD40 proteins to CUL4-ROC1 ubiquitin ligases. *Genes Dev.* **2006**, *20*, 2949−2954.

(12) Zhang, S.; Feng, Y.; Narayan, O.; Zhao, L. J. Cytoplasmic retention of HIV-1 regulatory protein Vpr by protein-protein interaction with a novel human cytoplasmic protein VprBP. *Gene* **2001**, *263*, 131−140.

(13) Tan, L.; Ehrlich, E.; Yu, X. F. DDB1 and Cul4A are required for human immunodeficiency virus type 1 Vpr-induced G2 arrest. *J. Virol.* **2007**, *81*, 10822−10830.

(14) Ahn, J.; Vu, T.; Novince, Z.; Guerrero-Santoro, J.; Rapic-Otrin, V.; Gronenborn, A. M. HIV-1 Vpr loads uracil DNA glycosylase-2 onto DCAF1, a substrate recognition subunit of a cullin 4A-ring E3 ubiquitin ligase for proteasome-dependent degradation. *J. Biol. Chem.* **2010**, *285*, 37333−37341.

(15) Klockow, L. C.; Sharifi, H. J.; Wen, X.; Flagg, M.; Furuya, A. K. M.; Nekorchuk, M.; de Noronha, C. M. C. The HIV-1 protein Vpr targets the endoribonuclease Dicer for proteasomal degradation to boost macrophage infection. *Virology* **2013**, *444*, 191−202.
(16) Zhou, X.; Monnie, C.; DeLucia, M.; Ahn, J. HIV-1 Vpr activates host CRL4-DCAF1 E3 ligase to degrade histone deacetylase SIRT7. *Virol. J.* **2021**, *18*, 48.
(17) Wu, Y.; Zhou, X.; Barnes, C. O.; DeLucia, M.; Cohen, A. E.; Gronenborn, A. M.; Ahn, J.; Calero, G. The DDB1-DCAF1-Vpr-UNG2 crystal structure reveals how HIV-1 Vpr steers human UNG2 toward destruction. *Nat. Struct. Mol. Biol.* **2016**, *23*, 933−940.
(18) Ahn, J.; Hao, C.; Yan, J.; DeLucia, M.; Mehrens, J.; Wang, C.; Gronenborn, A. M.; Skowronski, J. HIV/simian immunodeficiency virus (SIV) accessory virulence factor Vpx loads the host cell restriction factor SAMHD1 onto the E3 ubiquitin ligase complex CRL4DCAF1. *J. Biol. Chem.* **2012**, *287*, 12550−12558.
(19) Wei, W.; Guo, H.; Han, X.; Liu, X.; Zhou, X.; Zhang, W.; Yu, X. F. A novel DCAF1-binding motif required for Vpx-mediated degradation of nuclear SAMHD1 and Vpr-induced G2 arrest. *Cell. Microbiol.* **2012**, *14*, 1745−1756.
(20) Schabla, N. M.; Mondal, K.; Swanson, P. C. DCAF1 (VprBP): emerging physiological roles for a unique dual-service E3 ubiquitin ligase substrate receptor. *J. Mol. Cell Biol.* **2019**, *11*, 725−735.
(21) Jung, H. Y.; Wang, X.; Jun, S.; Park, J. I. Dyrk2-associated EDD-DDB1-VprBP E3 ligase inhibits telomerase by TERT degradation. *J. Biol. Chem.* **2013**, *288*, 7252−7262.
(22) Hossain, D.; Javadi Esfehani, Y.; Das, A.; Tsang, W. Y. Cep78 controls centrosome homeostasis by inhibiting EDD-DYRK2-DDB1-(Vpr)(BP). *EMBO Rep.* **2017**, *18*, 632−644.
(23) Hossain, D.; Barbosa, J. A. F.; Cohen, É. A.; Tsang, W. Y. HIV-1 Vpr hijacks EDD-DYRK2-DDB1(DCAF1) to disrupt centrosome homeostasis. *J. Biol. Chem.* **2018**, *293*, 9448−9460.
(24) Nakagawa, T.; Mondal, K.; Swanson, P. C. VprBP (DCAF1): a promiscuous substrate recognition subunit that incorporates into both RING-family CRL4 and HECT-family EDD/UBR5 E3 ubiquitin ligases. *BMC Mol. Biol.* **2013**, *14*, 22.
(25) Kim, K.; Kim, J. M.; Kim, J. S.; Choi, J.; Lee, Y. S.; Neamati, N.; Song, J. S.; Heo, K.; An, W. VprBP has intrinsic kinase activity targeting histone H2A and represses gene transcription. *Mol. Cell* **2013**, *52*, 459−467.
(26) Ghate, N. B.; Kim, S.; Spiller, E.; Kim, S.; Shin, Y.; Rhie, S. K.; Smbatyan, G.; Lenz, H. J.; Mumenthaler, S. M.; An, W. VprBP directs epigenetic gene silencing through histone H2A phosphorylation in colon cancer. *Mol. Oncol.* **2021**, *15*, 2801−2817.
(27) McCloskey, K.; Sigel, E. A.; Kearnes, S.; Xue, L.; Tian, X.; Moccia, D.; Gikunju, D.; Bazzaz, S.; Chan, B.; Clark, M. A.; Cuozzo, J. W.; Guié, M.-A.; Guilinger, J. P.; Huguet, C.; Hupp, C. D.; Keefe, A. D.; Mulhern, C. J.; Zhang, Y.; Riley, P. Machine Learning on DNA-Encoded Libraries: A New Paradigm for Hit Finding. *J. Med. Chem.* **2020**, *63*, 8857−8866.
(28) Cuozzo, J. W.; Centrella, P. A.; Gikunju, D.; Habeshian, S.; Hupp, C. D.; Keefe, A. D.; Sigel, E. A.; Soutter, H. H.; Thomson, H. A.; Zhang, Y.; Clark, M. A. Discovery of a Potent BTK Inhibitor with a Novel Binding Mode by Using Parallel Selections with a DNA-Encoded Chemical Library. *ChemBioChem* **2017**, *18*, 864−871.
(29) Bissantz, C.; Kuhn, B.; Stahl, M. A medicinal chemist's guide to molecular interactions. *J. Med. Chem.* **2010**, *53*, 5061−5084.
(30) Schwinn, M. K.; Machleidt, T.; Zimmerman, K.; Eggers, C. T.; Dixon, A. S.; Hurst, R.; Hall, M. P.; Encell, L. P.; Binkowski, B. F.; Wood, K. V. CRISPR-Mediated Tagging of Endogenous Proteins with a Luminescent Peptide. *ACS Chem. Biol.* **2018**, *13*, 467−474.
(31) Tao, Y.; Remillard, D.; Vinogradova, E. V.; Yokoyama, M.; Banchenko, S.; Schwefel, D.; Melillo, B.; Schreiber, S. L.; Zhang, X.; Cravatt, B. F. Targeted Protein Degradation by Electrophilic PROTACs that Stereoselectively and Site-Specifically Engage DCAF1. *J. Am. Chem. Soc.* **2022**, *144*, 18688−18699.
(32) Li, W.; Cooper, J.; Zhou, L.; Yang, C.; Erdjument-Bromage, H.; Zagzag, D.; Snuderl, M.; Ladanyi, M.; Hanemann, C. O.; Zhou, P.; Karajannis, M. A.; Giancotti, F. G. Merlin/NF2 loss-driven tumorigenesis linked to CRL4(DCAF1)-mediated inhibition of the hippo pathway kinases Lats1 and 2 in the nucleus. *Cancer Cell* **2014**, *26*, 48−60.
(33) Li, W.; You, L.; Cooper, J.; Schiavon, G.; Pepe-Caprio, A.; Zhou, L.; Ishii, R.; Giovannini, M.; Hanemann, C. O.; Long, S. B.; Erdjument-Bromage, H.; Zhou, P.; Tempst, P.; Giancotti, F. G. Merlin/NF2 suppresses tumorigenesis by inhibiting the E3 ubiquitin ligase CRL4(DCAF1) in the nucleus. *Cell* **2010**, *140*, 477−490.
(34) Cooper, J.; Li, W.; You, L.; Schiavon, G.; Pepe-Caprio, A.; Zhou, L.; Ishii, R.; Giovannini, M.; Hanemann, C. O.; Long, S. B.; Erdjument-Bromage, H.; Zhou, P.; Tempst, P.; Giancotti, F. G. Merlin/NF2 functions upstream of the nuclear E3 ubiquitin ligase CRL4DCAF1 to suppress oncogenic gene expression. *Sci. Signaling* **2011**, *4*, pt6.
(35) Schneider, N.; Lange, G.; Hindle, S.; Klein, R.; Rarey, M. A consistent description of HYdrogen bond and DEhydration energies in protein-ligand complexes: methods behind the HYDE scoring function. *J. Comput.-Aided Mol. Des.* **2013**, *27*, 15−29.
(36) Hutchinson, A.; Seitova, A. Production of Recombinant PRMT Proteins using the Baculovirus Expression Vector System. *J. Visualized Exp.* **2021**, *173*, No. e62510.
(37) Kabsch, W. Xds. *Acta Crystallogr., Sect. D: Biol. Crystallogr.* **2010**, *66*, 125−132.
(38) Evans, P. R.; Murshudov, G. N. How good are my data and what is the resolution? *Acta Crystallogr., Sect. D: Biol. Crystallogr.* **2013**, *69*, 1204−1214.
(39) McCoy, A. J.; Grosse-Kunstleve, R. W.; Adams, P. D.; Winn, M. D.; Storoni, L. C.; Read, R. J. Phaser crystallographic software. *J. Appl. Crystallogr.* **2007**, *40*, 658−674.
(40) Minor, W.; Cymborowski, M.; Otwinowski, Z.; Chruszcz, M. HKL-3000: the integration of data reduction and structure solution–from diffraction images to an initial model in minutes. *Acta Crystallogr., Sect. D: Biol. Crystallogr.* **2006**, *62*, 859−866.
(41) Emsley, P.; Cowtan, K. Coot: model-building tools for molecular graphics. *Acta Crystallogr., Sect. D: Biol. Crystallogr.* **2004**, *60*, 2126−2132.
(42) Murshudov, G. N.; Vagin, A. A.; Dodson, E. J. Refinement of macromolecular structures by the maximum-likelihood method. *Acta Crystallogr., Sect. D: Biol. Crystallogr.* **1997**, *53*, 240−255.
(43) Winn, M. D.; Ballard, C. C.; Cowtan, K. D.; Dodson, E. J.; Emsley, P.; Evans, P. R.; Keegan, R. M.; Krissinel, E. B.; Leslie, A. G. W.; McCoy, A.; McNicholas, S. J.; Murshudov, G. N.; Pannu, N. S.; Potterton, E. A.; Powell, H. R.; Read, R. J.; Vagin, A.; Wilson, K. S. Overview of the CCP4 suite and current developments. *Acta Crystallogr., Sect. D: Biol. Crystallogr.* **2011**, *67*, 235−242.
(44) Chen, V. B.; Arendall, W. B., III; Headd, J. J.; Keedy, D. A.; Immormino, R. M.; Kapral, G. J.; Murray, L. W.; Richardson, J. S.; Richardson, D. C. MolProbity: all-atom structure validation for macromolecular crystallography. *Acta Crystallogr., Sect. D: Biol. Crystallogr.* **2010**, *66*, 12−21.
(45) Stierand, K.; Maass, P. C.; Rarey, M. Molecular complexes at a glance: automated generation of two-dimensional complex diagrams. *Bioinformatics* **2006**, *22*, 1710−1716.
(46) Pettersen, E. F.; Goddard, T. D.; Huang, C. C.; Couch, G. S.; Greenblatt, D. M.; Meng, E. C.; Ferrin, T. E. UCSF Chimera–a visualization system for exploratory research and analysis. *J. Comput. Chem.* **2004**, *25*, 1605−1612.
(47) DeLano, W. L. *PyMOL*; 2002.

https://doi.org/10.1021/acs.jmedchem.2c02132
J. Med. Chem. 2023, 66, 5041−5060